NACA RM A51E24

NACA

RESEARCH MEMORANDUM

AN EXPERIMENTAL INVESTIGATION AT SUBSONIC SPEEDS OF A SCOOP-TYPE AIR-INDUCTION SYSTEM FOR A SUPERSONIC AIRPLANE

By Curt A. Holzhauser

Ames Aeronautical Laboratory
Moffett Field, Calif.

NATIONAL ADVISORY COMMITTEE
FOR AERONAUTICS

WASHINGTON
July 19, 1951

 [redacted] UNCLASSIFIED

NATIONAL ADVISORY COMMITTEE FOR AERONAUTICS

RESEARCH MEMORANDUM

AN EXPERIMENTAL INVESTIGATION AT SUBSONIC SPEEDS OF A SCOOP-TYPE AIR-INDUCTION SYSTEM FOR A SUPERSONIC AIRPLANE

By Curt A. Holzhauser

SUMMARY

An investigation was made at subsonic speeds of a scoop-type air-induction system designed for use at subsonic and supersonic speeds. Measurements were made of the ram-recovery ratio and static pressures in a scoop-type intake mounted on the upper surface of the fuselage and of the static pressures and boundary layer along the upper surface of the fuselage forebody. These measurements were made for a large range of mass-flow ratios, angles of attack, and angles of sideslip.

At 0° angles of attack and sideslip, the ram-recovery ratio measured at the minimum-area station in the duct (6.88 inches downstream from the entrance) was greater than 0.95 between mass-flow ratios of 0.2 and 1.2. Above a mass-flow ratio of 1.2, the ram-recovery ratio decreased rapidly with increasing mass-flow ratio.

By visual observation of smoke filaments, vortices were seen to form from the forebody with the fuselage at angles of attack greater than 6°. These vortices acted as boundary-layer-control devices in that they reduced the boundary-layer thickness on the upper surface of the forebody above 6° angle of attack. This reduction resulted in a small variation of ram-recovery ratio with angle of attack as compared to the variation of ram-recovery ratio with angle of sideslip. For the scoop-type air-induction system investigated, it is advantageous to locate the intake on the top or bottom rather than on the side of the fuselage.

INTRODUCTION

Many air-induction systems suitable for supersonic airplanes or missiles have been tested at supersonic speeds. These systems were generally designed to give high net thrust at the supersonic speeds by

[redacted]

the use of geometrical features such as sharp leading edges on the intake, ramps or cones in front of the intake, and internal contraction in the duct. One of the installations that was found to be moderately satisfactory at supersonic speeds was the twin-scoop air-induction system of reference 1. For this installation, total-pressure recoveries were obtained that approached the values for a normal shock at the test Mach numbers of 1.36 to 2.01. To attain these supersonic speeds, the airplane must successfully fly through the subsonic-speed range. Therefore, it is necessary to know the characteristics of the air-induction system at subsonic speeds to determine what design compromises are necessary.

The tests for the study reported herein were performed in one of the Ames 7- by 10-foot wind tunnels with a model similar to that of reference 1. Measurements of the static pressure and total pressure in the top duct and the boundary-layer profiles on the forebody were made at a free-stream Mach number of 0.17 for a wide range of mass-flow ratios, angles of attack, and angles of sideslip. This investigation is the first of several studies at the Ames Laboratory to determine the subsonic characteristics of air-induction systems designed for supersonic airplanes.

NOTATION

a speed of sound, feet per second

A duct area, square feet

D maximum diameter of forebody, inches

H total pressure, pounds per square foot

$\frac{m_1}{m_o}$ ratio of the mass of air in the duct to the mass of air in the free stream passing through an area equal to the area of the intake $\left(\frac{\rho_1 A_1 V_1}{\rho_o A_1 V_o} \right)$

M Mach number $\left(\frac{V}{a} \right)$

p static pressure, pounds per square foot

P static-pressure coefficient $\left(\frac{p - p_o}{q_o} \right)$

[redacted]

q dynamic pressure $\left(\frac{1}{2}\rho V^2\right)$, pounds per square foot

u velocity in the boundary layer, feet per second

U local velocity outside of the boundary layer, feet per second

V velocity of the air stream, feet per second

y distance from the surface to a point in the boundary layer, inches

α angle of attack referred to fuselage center line, degrees

β angle of sideslip referred to fuselage center line, degrees

δ boundary-layer thickness, where the velocity in the boundary layer is 0.99 of the local velocity outside of the boundary layer, inches

δ^* displacement thickness of the boundary layer $\left[\int_0^{\delta}\left(1 - \frac{u}{U}\right) dy\right]$, inches

η diffuser efficiency $\left[1 - \left(\frac{H_2 - H_3}{q_2}\right)\right]$

θ momentum thickness of the boundary layer $\left[\int_0^{\delta}\frac{u}{U}\left(1 - \frac{u}{U}\right)dy\right]$, inches

ρ mass density of the air, slugs per cubic foot

Subscripts

0 free stream

1 duct station 1 (duct entrance)

2 duct station 2 (minimum-area station)

3 duct station 3 (compressor inlet)

[redacted]

DESIGN CONSIDERATIONS AND DESCRIPTION OF THE MODEL

The proportions of the model in the present investigation were selected after making a preliminary study of proposed designs of supersonic airplanes with axial-flow turbojet engines. The proportions selected are those of an airplane designed for a flight Mach number of 1.7 at an altitude of 28,000 feet using two engines each developing 6000 pounds of static thrust at sea level. The design employed had a ratio of intake area to fuselage frontal area of 0.15. The location and general configuration of the intakes were similar to those of the twin-scoop air-induction system reported in reference 1.

To allow utilization of the space in the nose, the air intakes were aft of the nose apex a distance of five maximum forebody diameters. The forebody, that portion of the fuselage ahead of the intakes, was comprised of an ogival nose followed by a cylindrical section. The profile of the nose was formed by two segments of a circle having a radius ten times the maximum forebody diameter; the distance from the apex of the segments to the point of tangency with the cylindrical section was 3.12 times the maximum forebody diameter. Each intake had a height-to-width ratio of 0.8, and the height was such that the oblique shock wave formed by the 12° ramp would intersect the top of the intake at a flight Mach number of 1.7. At this design Mach number the speed of the air entering the intake would be supersonic; therefore, a sharp leading edge was used in conjunction with a convergent-divergent diffuser. The convergent section of the diffuser had a constant rate of decrease of area along its length; the divergent section of the diffuser had a constant rate of increase of area along its length. To maintain this change in area without abrupt changes in duct contour a fairing was placed over the simulated accessory housing of the engine.

Figures 1 and 2 show the model mounted in the wind tunnel with the intakes on the top and bottom of the model. A schematic drawing showing the general arrangement and pertinent dimensions of the model is presented in figure 3. Figure 4 shows the cross-sectional shapes and the duct areas of the upper half of the fuselage at duct stations 1, 2, and 3.

APPARATUS

The model was mounted on an 8-inch pipe which was attached to the turntable in the floor of the wind tunnel. The air flow through the model was controlled by a variable-speed centrifugal blower. The quantity of air flow was measured by a standard ASME orifice meter.

Pressure-recovery measurements were made at the minimum-area station (duct station 2) and at the compressor inlet station (duct station 3). The rake at the minimum-area station consisted of 40 total-pressure tubes and 18 static-pressure tubes; the rake at the compressor inlet consisted of 76 total-pressure tubes and 8 static-pressure tubes. The latter rake was attached to the simulated accessory housing.

The static-pressure distributions on the forebody, on the duct floor, and on the duct roof were determined from measurements made by flush orifices. These orifices were connected to a water-in-glass multiple-tube manometer.

Boundary-layer measurements were made along the forebody in a plane passing through the center line of the duct. The rake used to make boundary-layer measurements consisted of 16 unequally spaced total-pressure tubes and 3 unequally spaced static-pressure tubes.

All total-pressure tubes and static-pressure tubes of the rakes were connected to water-in-glass multiple-tube manometers. The total-pressure distributions as well as the static-pressure distributions were recorded photographically.

TESTS

A preliminary investigation indicated that the measurements of static pressures and total pressures in the top duct were unaffected by the flow changes resulting from the duct on the bottom being blocked at the compressor inlet; therefore, all results reported herein are for the top inlet only with the bottom duct blocked at the compressor station. Data were obtained in the top duct at a free-stream Mach number of 0.17 for a mass-flow-ratio range of 0 to 4.0 with the model at 0° angle of attack and 0° angle of sideslip, and at mass-flow ratios of 0.6, 1.0, 1.6, and 2.2 throughout an angle-of-sideslip range of 0° to 21° at 0°, 10°, and -10° angles of attack with the model mounted as shown in figure 1. By rotating the model 90° to the attitude shown in figure 2, data were taken at mass-flow ratios of 0.6, 1.0, 1.6, and 2.2 throughout an angle-of-attack range of -21° to 21° at 0° and 10° angles of sideslip. By comparing the ram-recovery ratios for equivalent conditions of mass-flow ratio, angle of attack, and angle of sideslip, it was ascertained that the pressure recovery of the intake was unaltered when the model was rotated 90°. The sign convention used for the various model attitudes is for a fuselage with the intakes on the top and bottom, with the top intake being investigated. (See fig. 5.)

When the ram-recovery ratio at the compressor inlet was measured, the rake at the minimum-area station was removed.

[redacted]

Boundary-layer measurements were made on the upper surface of the forebody at a free-stream Mach number of 0.17 for several mass-flow ratios at various angles of attack with the model at 0° angle of sideslip.

When the fuselage was at a positive angle of attack, the air flow over the forebody was visualized by smoke at a Mach number of approximately 0.01. In these studies the smoke was ejected through orifices in the side of the fuselage, and the stream filaments were illuminated in a vertical plane by a slit of light of high intensity. The air flow over the forebody and over the forward portion of the intake was observed by using tufts at a Mach number of 0.17.

RESULTS

Ram-Recovery Ratio

The effect of mass-flow ratio on the ram-recovery ratio at the minimum-area section (duct station 2) is shown in figure 6 for a mass-flow-ratio range of 0 to 1.9. In this figure the area-weighted ram-recovery ratio and the mass-flow-weighted ram-recovery ratio are shown. The area-weighted ram-recovery ratio was obtained by weighting the total pressure indicated by each tube according to the area apportioned to that tube. The mass-flow-weighted ram-recovery ratio was calculated in the manner set forth in reference 2 in which the total pressure indicated by each tube was weighted according to the mass of air flowing through the area apportioned to that tube.

The effect of mass-flow ratio on the area weighted and on the mass-flow-weighted ram-recovery ratio measured at the compressor inlet (duct station 3) is shown in figure 7(a) for a mass-flow-ratio range of 0 to 2.0 and in figure 7(b) for a mass-flow-ratio range of 0 to 4.0 for the model at 0° angle of attack and 0° angle of sideslip. In these figures it is seen that the difference between the values of ram-recovery ratio calculated by the two methods increased with increasing mass-flow ratio. The area-weighted ram-recovery ratio was less than the mass-flow-weighted ram-recovery ratio, and the differences in the ram-recovery ratio at the compressor inlet computed by these two methods were small at the lower mass-flow ratios for the model at 0° angle of attack and 0° angle of sideslip. It was felt that the additional work required to compute the mass-flow-weighted ram-recovery ratios was not justified at other than at 0° angles of attack and sideslip. In general, the variation in the distribution of ram-recovery ratio at the compressor inlet increased with angle of attack and angle of sideslip; therefore, the difference between the area weighted and the

[redacted]

mass-flow-weighted ram-recovery ratio would increase as the angle of attack or angle of sideslip were varied from 0°.

As can be seen in figure 8, the average value of the efficiency of the divergent portion of the diffuser, $1 - \left(\frac{H_2-H_3}{q_2}\right)$, was approximately 92 percent. The variation of the diffuser efficiency with mass-flow ratio was small.

Figure 9(a) presents the effect of angle of attack on the ram-recovery ratio at the compressor inlet for mass-flow ratios of 0.6, 1.0, 1.6, and 2.2 for the model at 0° and 10° angle of sideslip. Figure 9(b) is a portion of figure 9(a) with an expanded vertical scale to show more accurately the variation of ram-recovery ratio with angle of attack. Figure 10 shows the effect of angle of sideslip on the ram-recovery ratio measured at the compressor inlet for mass-flow ratios of 0.6, 1.0, 1.6, and 2.2 for the model at 0°, -10°, and 10° angles of attack.

The ram-recovery-ratio distributions at the minimum-area station and at the compressor inlet are given in figures 11 and 12, respectively, for various mass-flow ratios, various angles of attack, and various angles of sideslip. Figure 13 shows the total-pressure-ratio distribution at the compressor inlet for an infinite mass-flow ratio (M_O=0) with an entrance Mach number of 0.31. All these pressure distributions are viewed looking forward.

Static-Pressure Distribution

The surfaces along which the static pressures were measured are indicated by heavy lines on cross-sectional diagrams of the model in figures 14, 15, and 16. The distribution of static-pressure coefficient, P, on the forebody, on the duct floor, and on the duct roof is given in figure 14 for several mass-flow ratios with the model at 0° angle of attack and 0° angle of sideslip. Figure 15 shows the effect of angle of attack on these distributions of pressure coefficient at constant mass-flow ratios with the model at 0° angle of sideslip. The effect of angle of sideslip on these distributions of pressure coefficient at constant mass-flow ratios is given in figure 16 for the model at 0° angle of attack.

[redacted]

External Air Flow

In figure 17, the momentum thickness obtained from boundary-layer measurements made along the upper surface of the forebody at various fuselage stations is compared with the momentum thickness calculated from theory for the model at 0° angle of attack and 0° angle of sideslip. Between fuselage stations 0 and 17.5 the boundary layer was too thin to be measured accurately with the available apparatus. Two methods of computing the theoretical momentum thickness of the boundary layer were used; in both methods it was assumed that transition from laminar to turbulent flow occurred 15 inches from the beginning of the fuselage. One of the methods was based on the boundary-layer theory for a flat plate; whereas the other method took into consideration the shape and the velocity distribution along the forebody. In the latter method, the momentum thickness was calculated in the laminar region from the equations developed in reference 3 and in the turbulent region from the equations developed in references 4 and 5. These calculations were made at 3-inch intervals along the fuselage. The calculations were not made downstream of fuselage station 54 because of the presence of the ramp and intake.

In figure 18, the boundary-layer profiles obtained from measurements made at fuselage stations 26.5, 38.5, and 50.5 are shown. These profiles are compared with boundary-layer profiles of the form $u/U = (y/\delta)^{1/7}$ to demonstrate that fully developed turbulent flow existed on this portion of the forebody at 0° angles of attack and sideslip. The variation of the displacement thickness and momentum thickness with angle of attack at fuselage stations 26.5, 38.5, and 50.5 is presented in figure 19 for the model at 0° angle of sideslip. As the angle of attack of the fuselage was decreased below -8° the measurements of the boundary layer became less accurate because the boundary-layer thickness decreased; therefore, the calculated values of displacement and momentum thickness below -8° angle of attack were omitted from this figure. The effect of angle of attack on the boundary-layer profile at fuselage station 50.5 is shown in figure 20. The photographs of the smoke study did not adequately portray the air flow over the forebody; therefore, the sketch presented in figure 21 was made to show the paths of several smoke filaments.

The air flow over the exterior of the intake is depicted by the photographs of tufts shown in figure 22 for several mass-flow ratios.

[redacted]

DISCUSSION

Ram-Recovery Ratio

At 0° angles of attack and sideslip the ram-recovery ratio at the minimum-area station (duct station 2) increased from 0.95 at a mass-flow ratio of 0.2 to 0.98 at a mass-flow ratio of 1.0 (fig. 6). Above a mass-flow ratio of 1.2, the rapid decrease in ram-recovery ratio with increasing mass-flow ratio was probably caused by separation of the air flow from the inside of the intake at or near its leading edge. This decrease in ram-recovery ratio was not accompanied by a large decrease in diffuser efficiency (fig. 8).

Comparison of the data in figures 9(a) and 10 indicates that the ram-recovery ratio decreased much more rapidly with increasing angle of sideslip than with increasing angle of attack. It is believed that the large decreases in ram-recovery ratio that occurred with the increasing angle of sideslip are the result of air-flow separation from the inside of the upwind side of the intake at or near its leading edge. Since airplanes in general undergo larger angle-of-attack changes for longer periods of time than angle-of-sideslip changes, and because the angles of attack and sideslip in this investigation are interchangeable, it is apparent that this type of inlet should be located on the top or bottom of a fuselage rather than on the sides.

External Air Flow

There was good agreement in the comparison of boundary-layer-momentum thickness along the upper surface of the forebody obtained from measurements and calculated from theory when the fuselage was at 0° angle of attack and 0° angle of sideslip. (See fig. 17.) The theoretical momentum thickness was calculated by two methods, using the boundary-layer equations for a flat plate and using the boundary-layer momentum equation adapted to radial flow. The latter equation takes into consideration the distribution of velocity along the fuselage and the divergence of the flow resulting from the shape of the forebody. The values of momentum thickness calculated by this method were in better agreement with the measured momentum thickness than the values calculated by flat-plate theory. From the measured boundary-layer profiles it was concluded that transition from laminar to turbulent flow occurred forward of fuselage station 17.5. For purposes of calculation, it was assumed that transition occurred at fuselage station 15, although it was found that assuming the transition point to be 3 inches forward or rearward of station 15 had little effect on the calculated momentum thickness behind fuselage station 40.

[redacted]

When the model was at an angle of attack, a pair of vortices formed from the inclined fuselage. These vortices were observed visually in this test by smoke studies. The vortices were equidistant from the vertical plane of symmetry, and their cores extended from near the beginning of the forebody to behind the entrance of the intake (fig. 21). The formation of vortices from an inclined body was observed at supersonic speeds (reference 6).

In figure 20, it is seen that at -3° angle of attack, which is lower than the angle of attack at which the vortices formed, the boundary-layer profile was similar to a one-seventh power turbulent-boundary-layer profile. At 6° angle of attack the profile deviated from the one-seventh power turbulent profile and approached the profile that exists prior to separation of a turbulent air flow. However, at 12° angle of attack, an angle at which the vortices were well established, a typical turbulent profile again existed. Thus it is concluded that the vortices precluded separation of the air flow from the top of the forebody.

At a given fuselage station and for a constant mass-flow ratio, the present experiments indicated that the effect of angle of attack on the boundary-layer-momentum thickness can be correlated qualitatively with its effect on ram-recovery ratio. As the angle of attack of the model was increased from a negative angle to about 6°, the boundary-layer-momentum thickness increased and the ram-recovery ratio decreased. (See figs. 19 and 9(b).) As the angle of attack of the model was increased further, the boundary-layer-momentum thickness decreased and the ram-recovery ratio increased.

Tuft studies with the model at 0° angle of attack and 0° angle of sideslip indicated that below a mass-flow ratio of 1.0 separation occurred on the outside surface of the intake at its leading edge. However, the flow reattached a short distance downstream and the flow was again smooth (fig. 22). This type of flow is typical of the separation of air flow from an airfoil with a sharp leading edge. The air flow over the exterior of the intake was unseparated at a mass-flow ratio of 1.0 and above.

CONCLUDING REMARKS

At the low subsonic Mach number of this investigation, the ram-recovery ratio at the minimum-area station was 0.98 at a mass-flow ratio of 1.0 with the model at 0° angles of attack and sideslip. Above a mass-flow ratio of 1.2 there was a sharp reduction in ram-recovery ratio. This reduction probably resulted from separation of the air flow from the inside of the intake at the leading edge. For the intake on top of

[redacted]

the fuselage, the variation of the ram-recovery ratio with angle of attack was small as compared to the variation of ram-recovery ratio with angle of sideslip. The reason for this comparatively small variation was that the boundary layer on top of the forebody was reduced in thickness by vortices forming from the forebody when the fuselage was at an angle of attack above 6°. It can be concluded from the results of the present investigation that the type of scoop tested should be on the top or bottom of a fuselage rather than on the sides.

Ames Aeronautical Laboratory,
National Advisory Committee for Aeronautics,
Moffett Field, Calif.

REFERENCES

1. Davis, Wallace F., Edwards, Sherman S., and Brajnikoff, George B.: Experimental Investigation at Supersonic Speeds of Twin-Scoop Duct Inlets of Equal Area. IV - Some Effects of Internal Duct Shape Upon an Inlet Enclosing 37.2 Percent of the Forebody Circumference. NACA RM A9A31, 1949.

2. Mossman, Emmet A., and Randall, Lauros M.: An Experimental Investigation of the Design Variables for NACA Submerged Duct Entrances. NACA RM A7I30, 1948.

3. Heaslet, Max. A., and Nitzberg, Gerald E.: The Calculation of Drag for Airfoil Sections and Bodies of Revolution at Subcritical Speeds. NACA RM A7B06, 1947.

4. Kehl, A.: Investigations on Convergent and Divergent Turbulent Boundary Layers. Ministry of Aircraft Production, R.T.P. Trans. 2035, Ingenier Archiv. Vol. XIII.

5. Tetervin, Neal: Boundary-Layer Momentum Equations for Three-Dimensional Flow. NACA TN 1479, 1947.

6. Allen, H. Julian, and Perkins, Edward W.: Characteristics of Flow Over Inclined Bodies of Revolution. NACA RM A50L07, 1951.

[redacted]

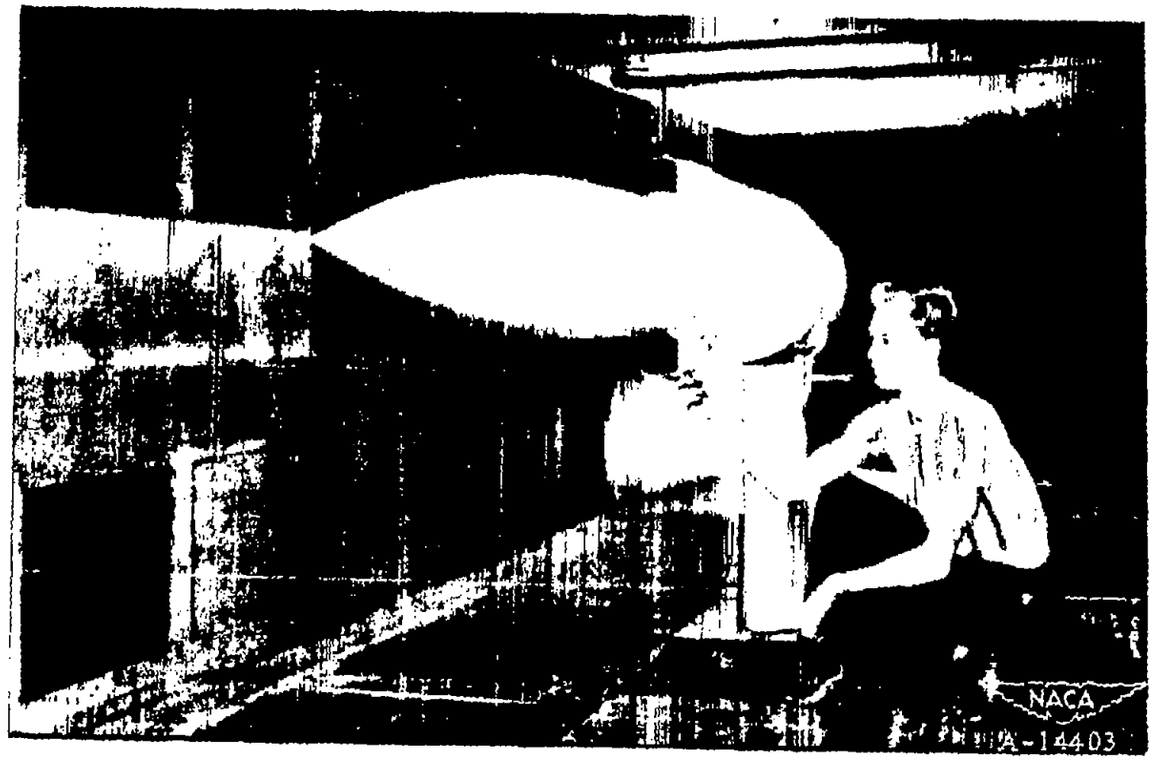

Figure 1.- The model with scoop-type intakes on the top and bottom.

Figure 2.- The model rotated 90° to permit testing at large angles of attack.

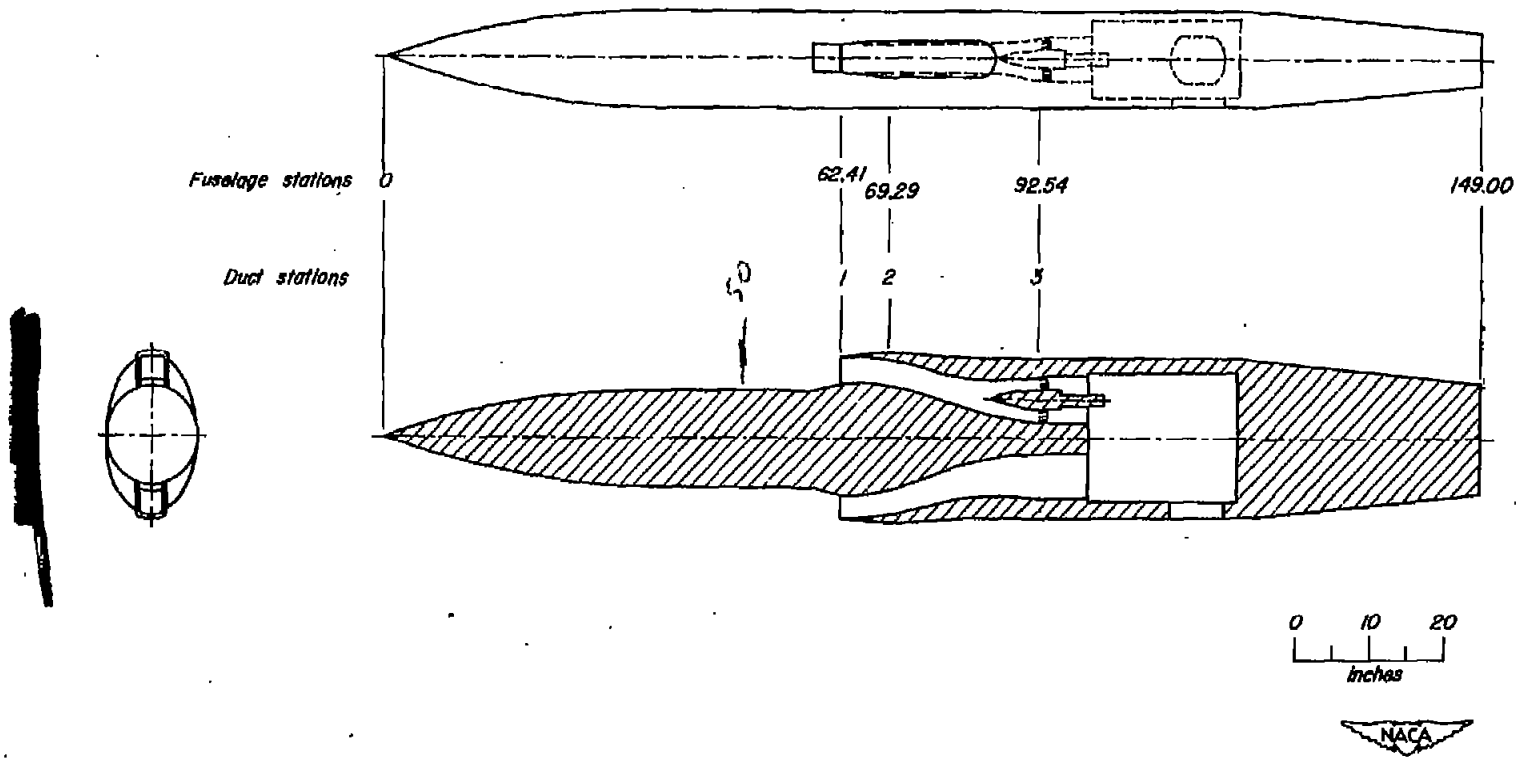

Figure 3.—Schematic drawing showing location of duct stations.

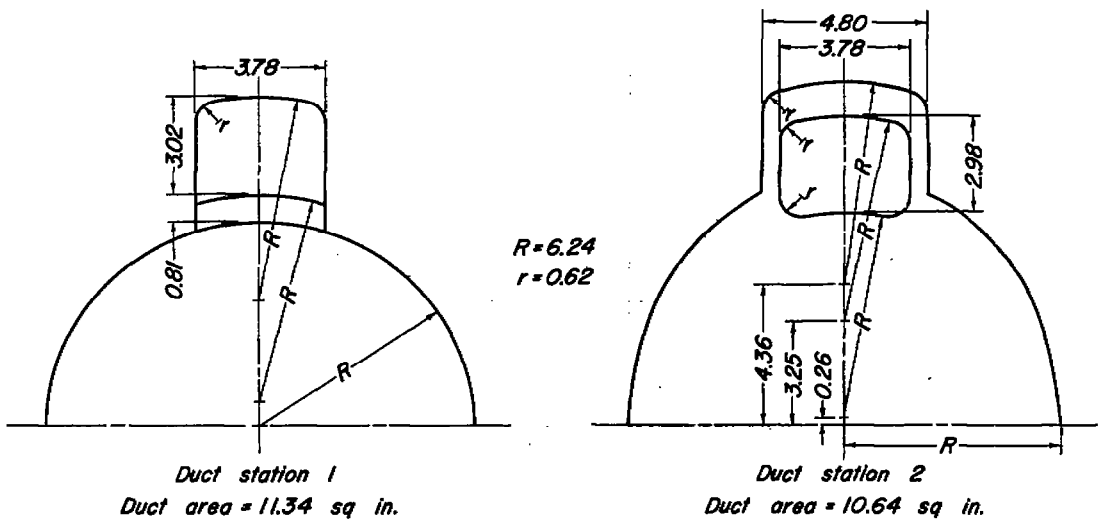

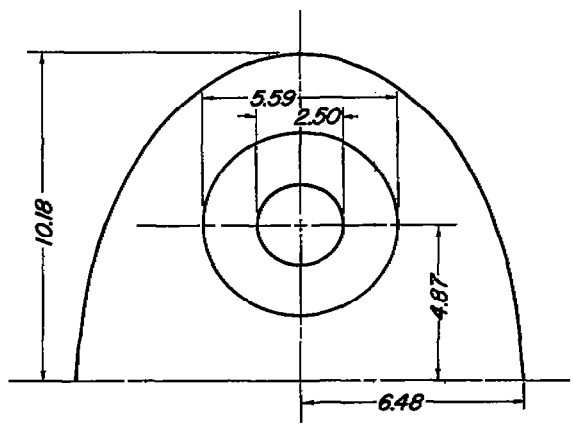

All dimensions are in inches.

Figure 4.— Cross sections and duct areas at duct stations 1, 2, and 3.

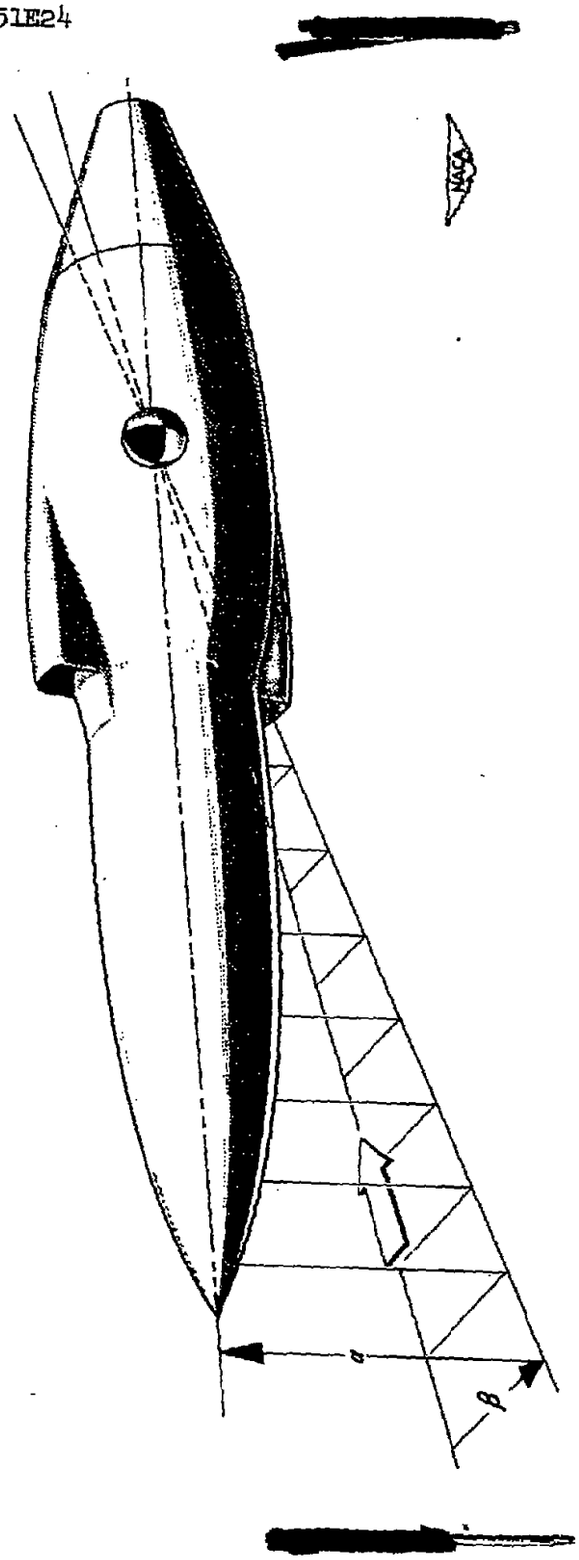

Figure 5.- Sketch showing positive directions for angle of attack and angle of sideslip.

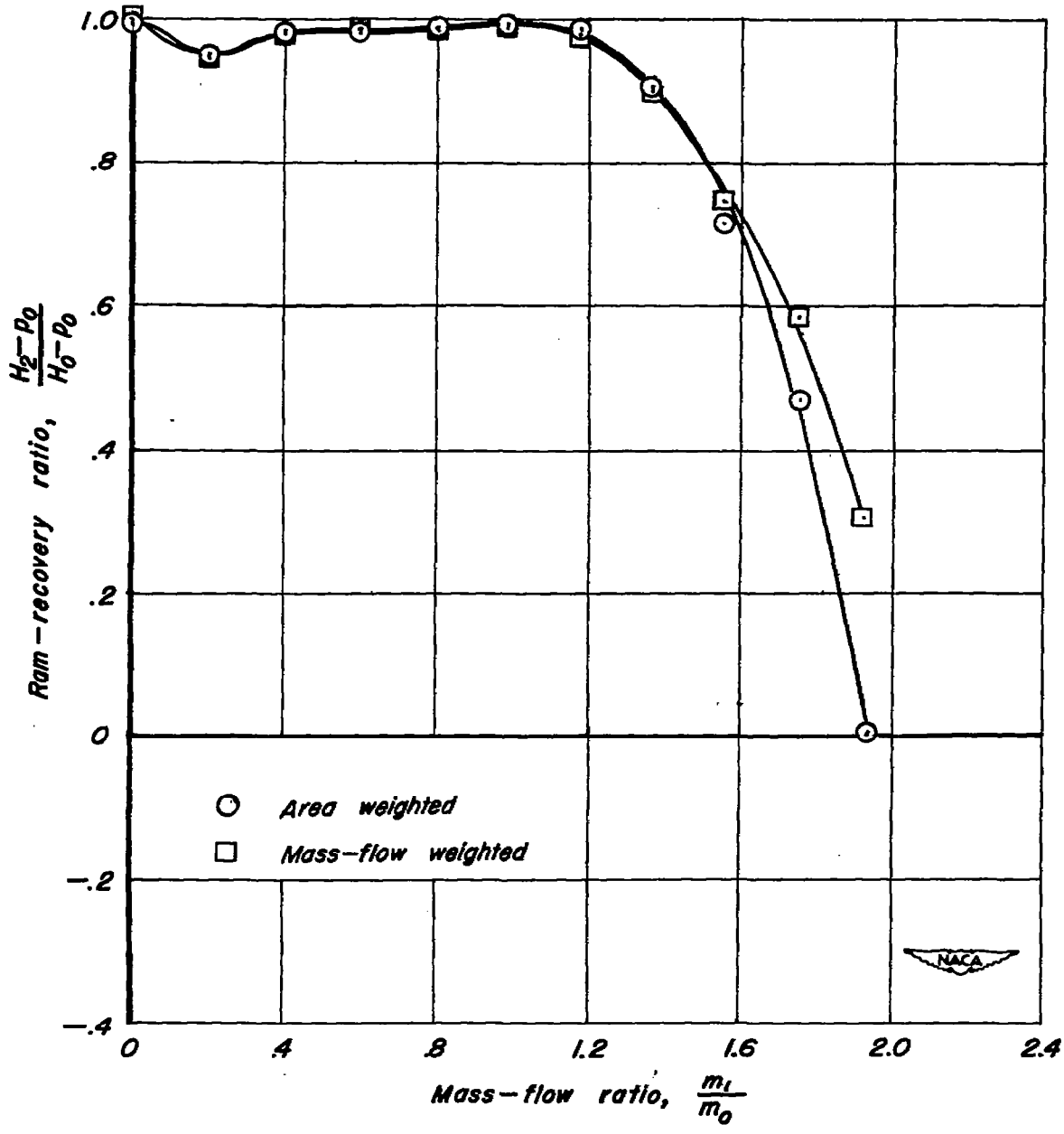

Figure 6.—The variation of ram−recovery ratio, measured at the minimum−area station, with mass−flow ratio; $\alpha = 0°$, $\beta = 0°$.

[redacted]

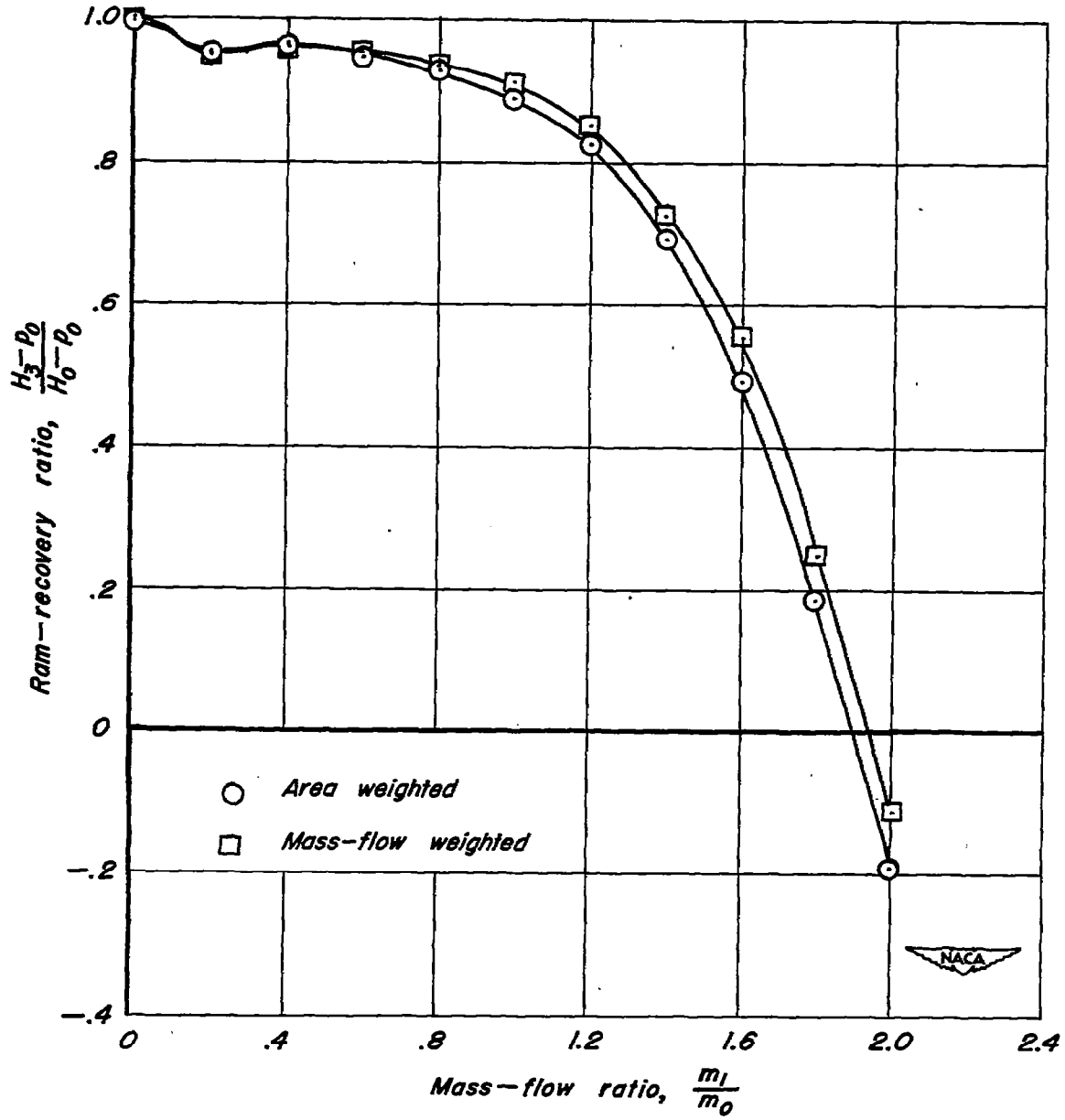

(a) Mass-flow-ratio range of 0 to 2.0.

Figure 7.—The variation of ram-recovery ratio, measured at the compressor-inlet station, with mass-flow ratio; $\alpha=0°$, $\beta=0°$.

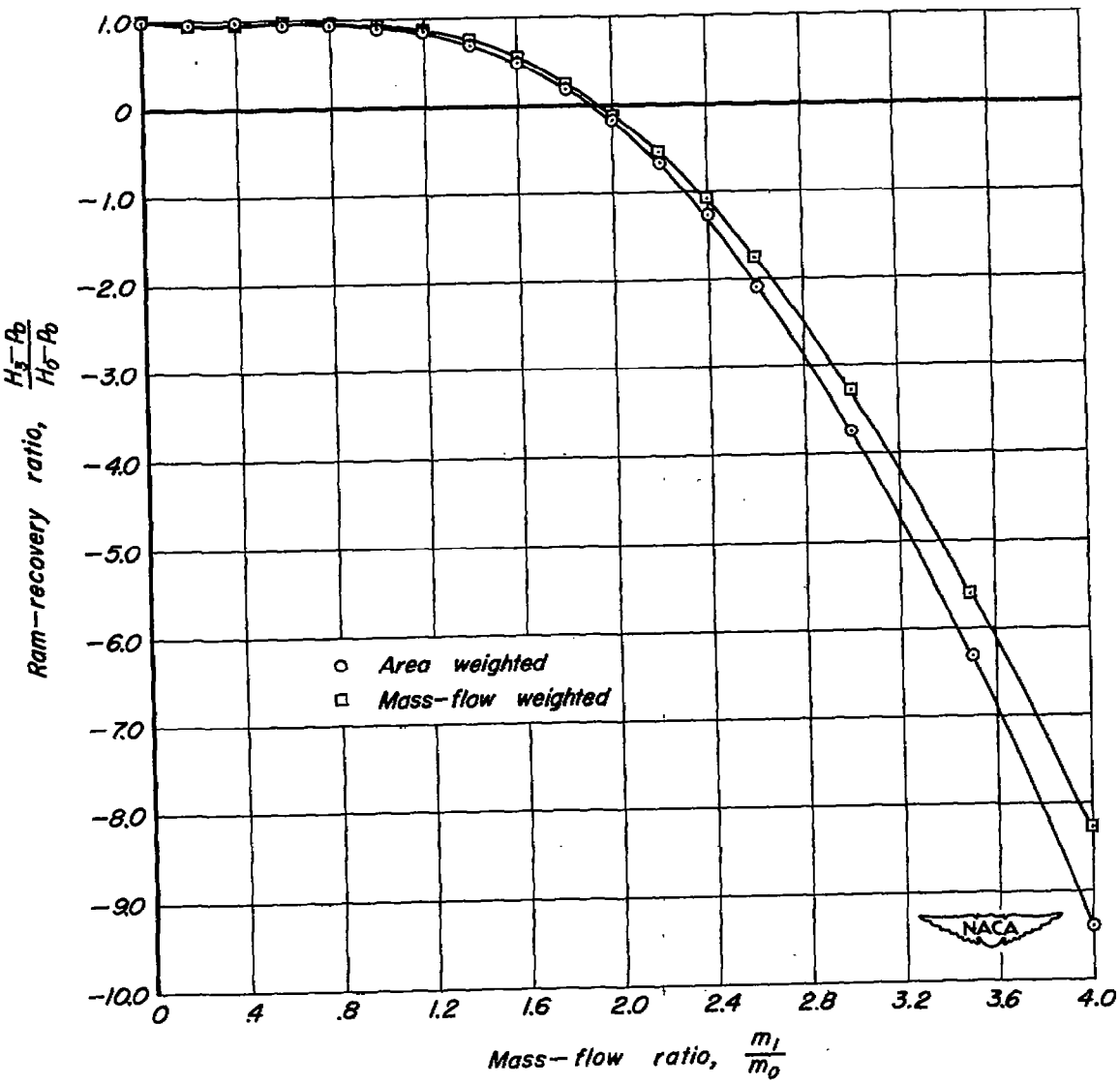

(b) Mass-flow-ratio range of 0 to 4.0.

Figure 7. – Concluded.

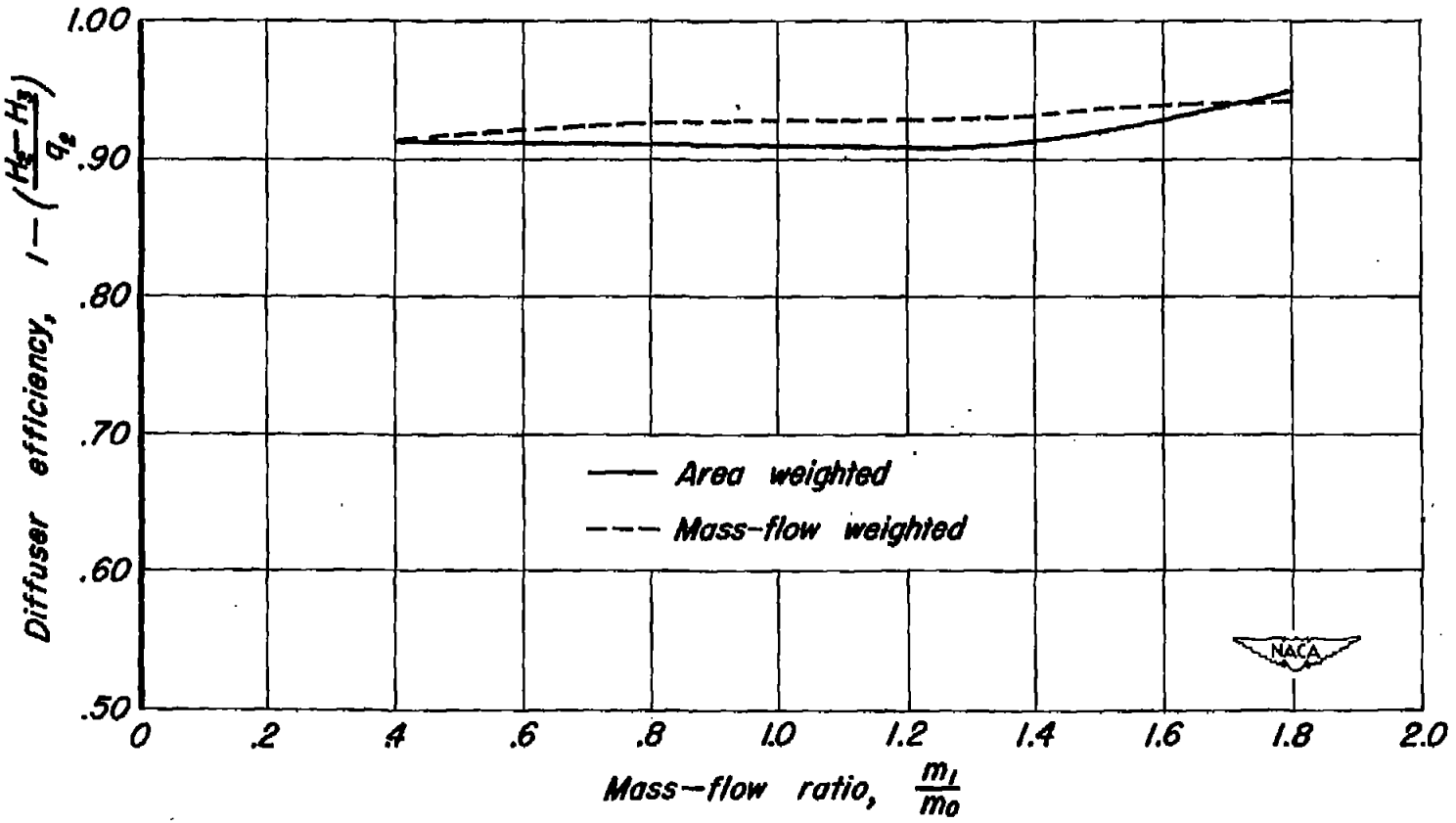

Figure 8.—The variation of diffuser efficiency with mass-flow ratio; $\alpha=0°$, $\beta=0°$.

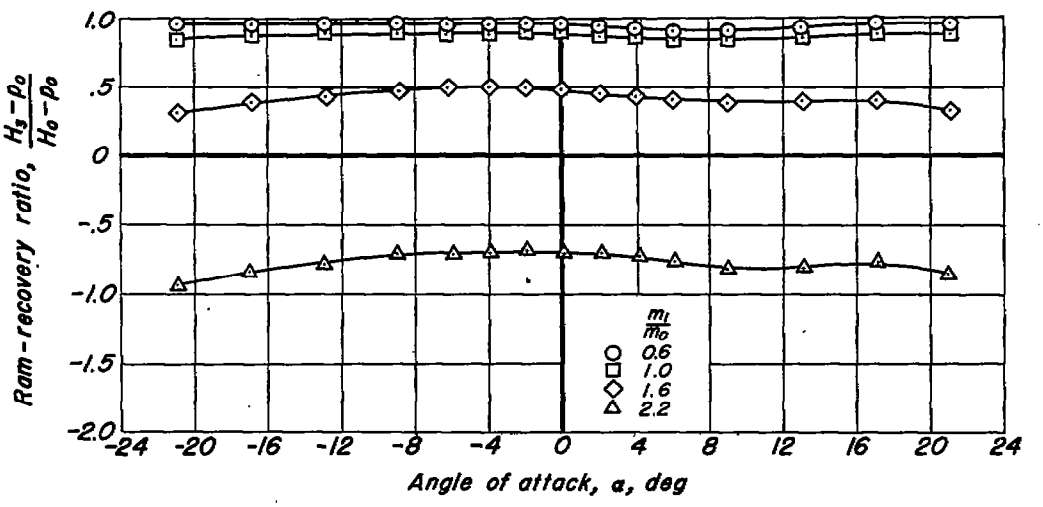

$\beta = 0°$

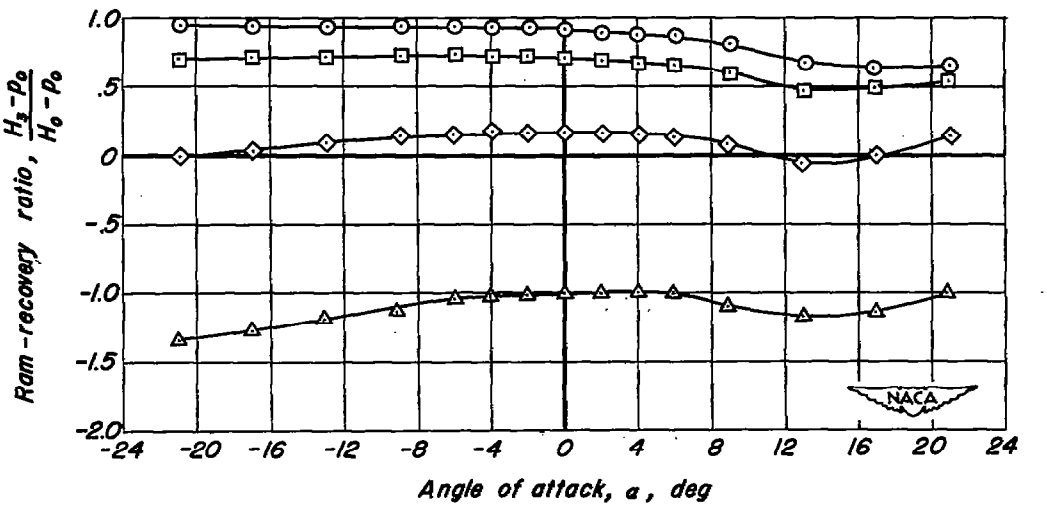

$\beta = 10°$

(a) $\frac{m_1}{m_0} = 0.6, 1.0, 1.6, 2.2$; $\beta = 0°, 10°$

Figure 9.—The effect of angle of attack on the ram-recovery ratio, measured at the compressor inlet, of the top intake.

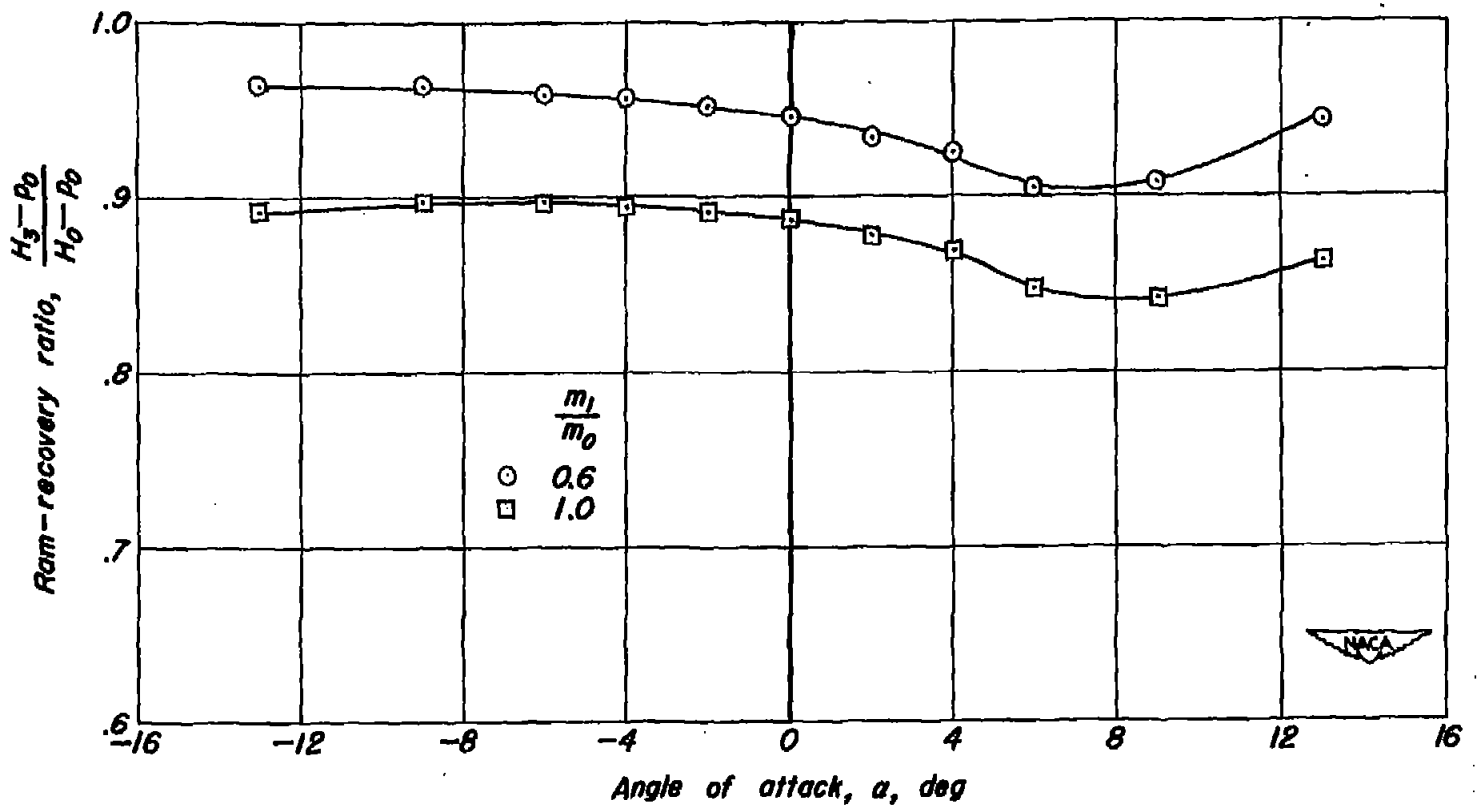

(b) $\frac{m_1}{m_0} = 0.6, 1.0; \beta = 0°$

Figure 9. —Concluded.

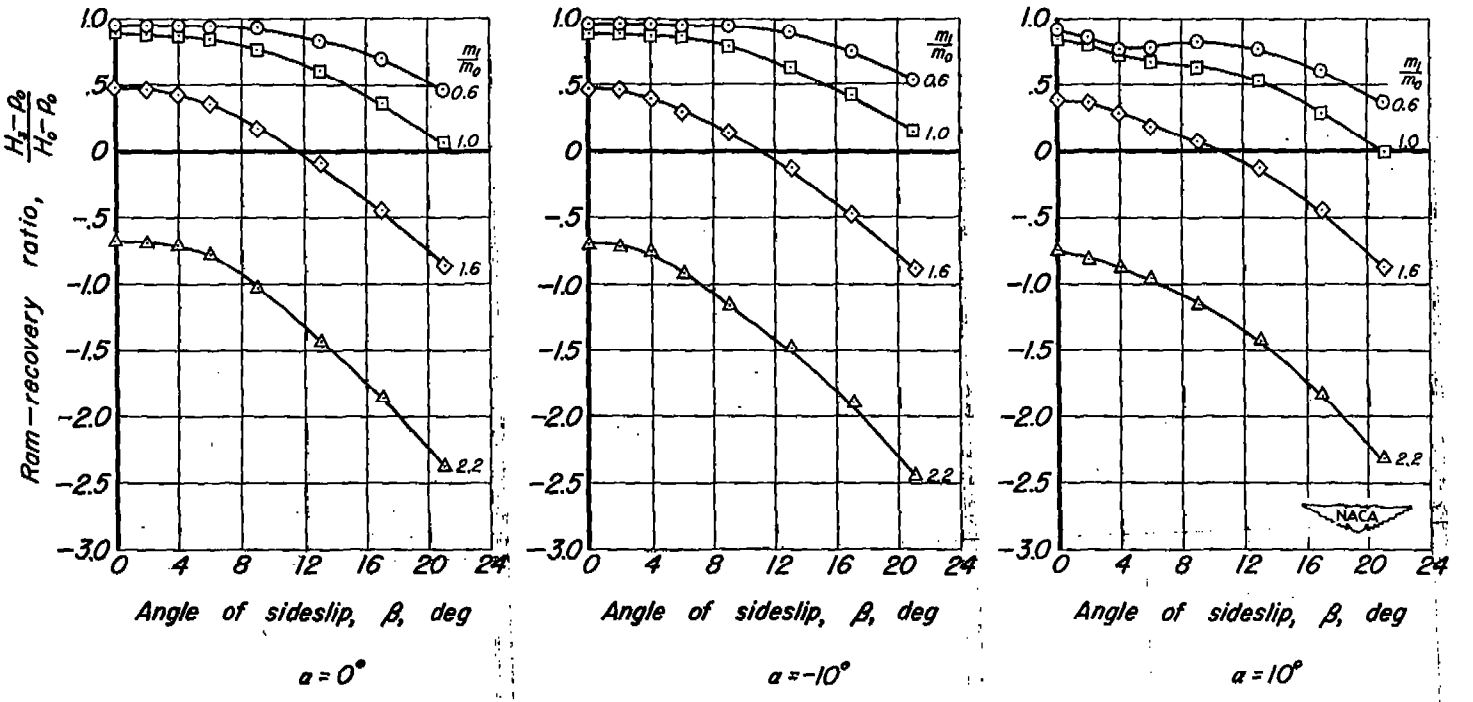

Figure 10.—The effect of angle of sideslip on the ram-recovery ratio, measured at the compressor inlet of the top intake.

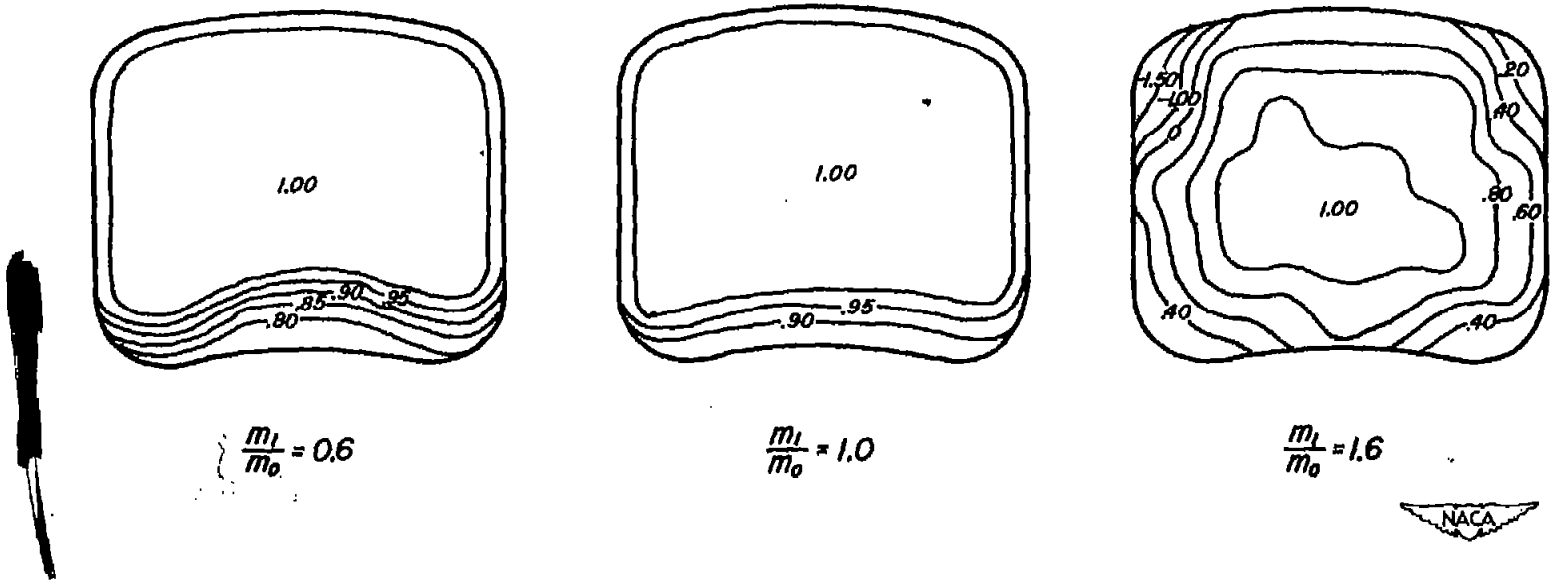

Figure 11.—Effect of mass-flow ratio on the distribution of ram-recovery ratio at the minimum area station; $\alpha = 0°$, $\beta = 0°$.

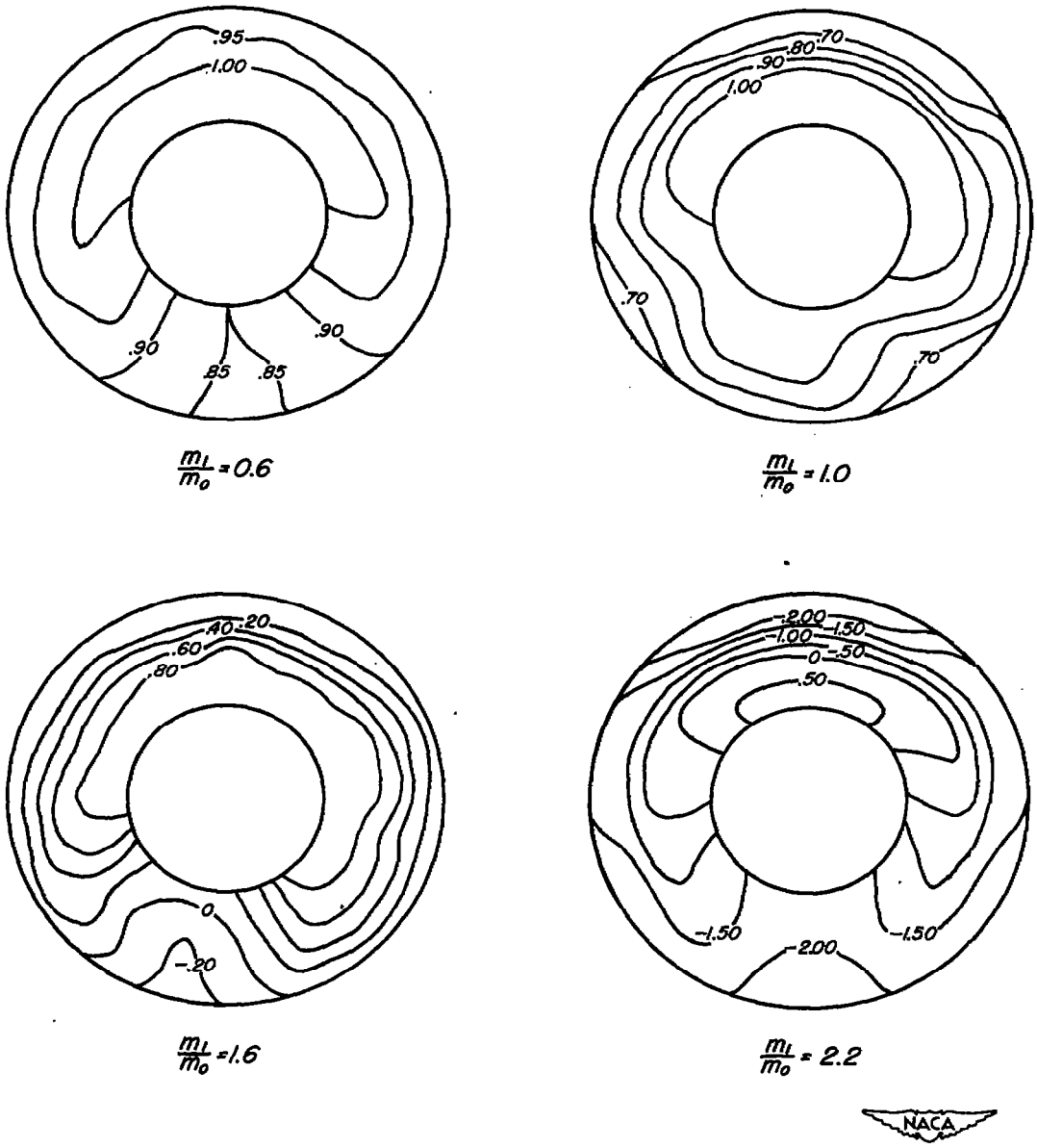

(a) Effect of mass-flow ratio; $\alpha=0°$, $\beta=0°$

Figure 12. – Distribution of ram–recovery ratio at compressor inlet as viewed looking upstream.

[redacted]

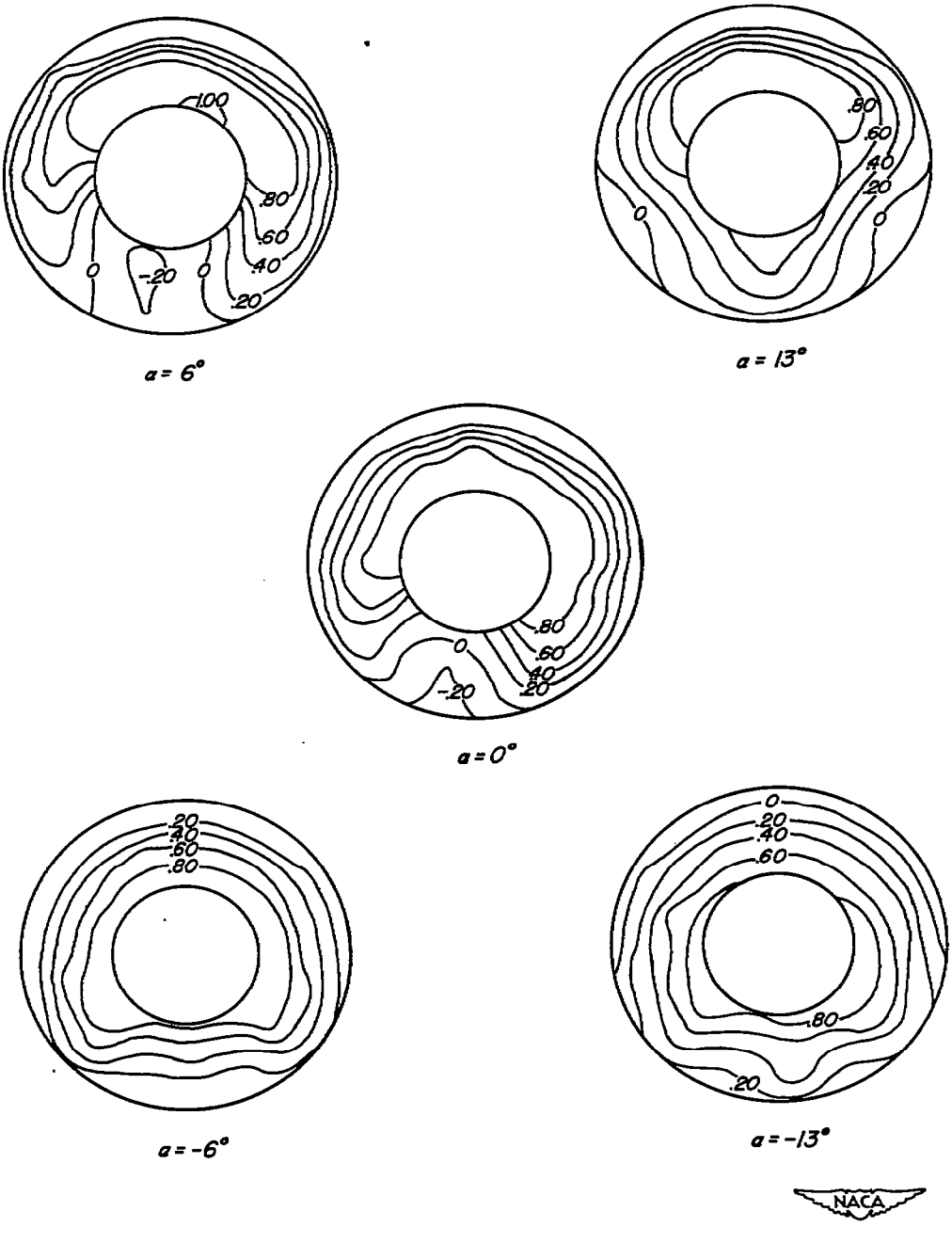

(b) Effect of angle of attack; $\frac{m_l}{m_o} = 1.0$, $\beta = 0°$

Figure 12.—Continued.

[redacted]

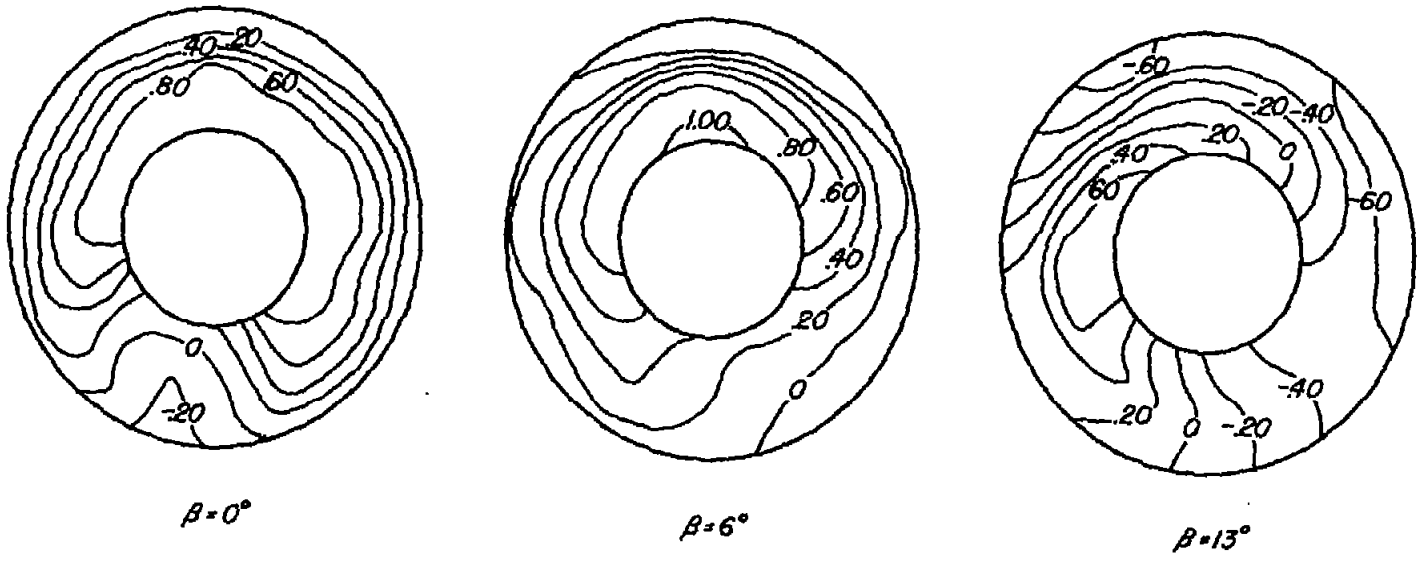

(c) Effect of angle of sideslip; $\frac{m_L}{m_0}$=1.0, α=0°

Figure 12.—Concluded.

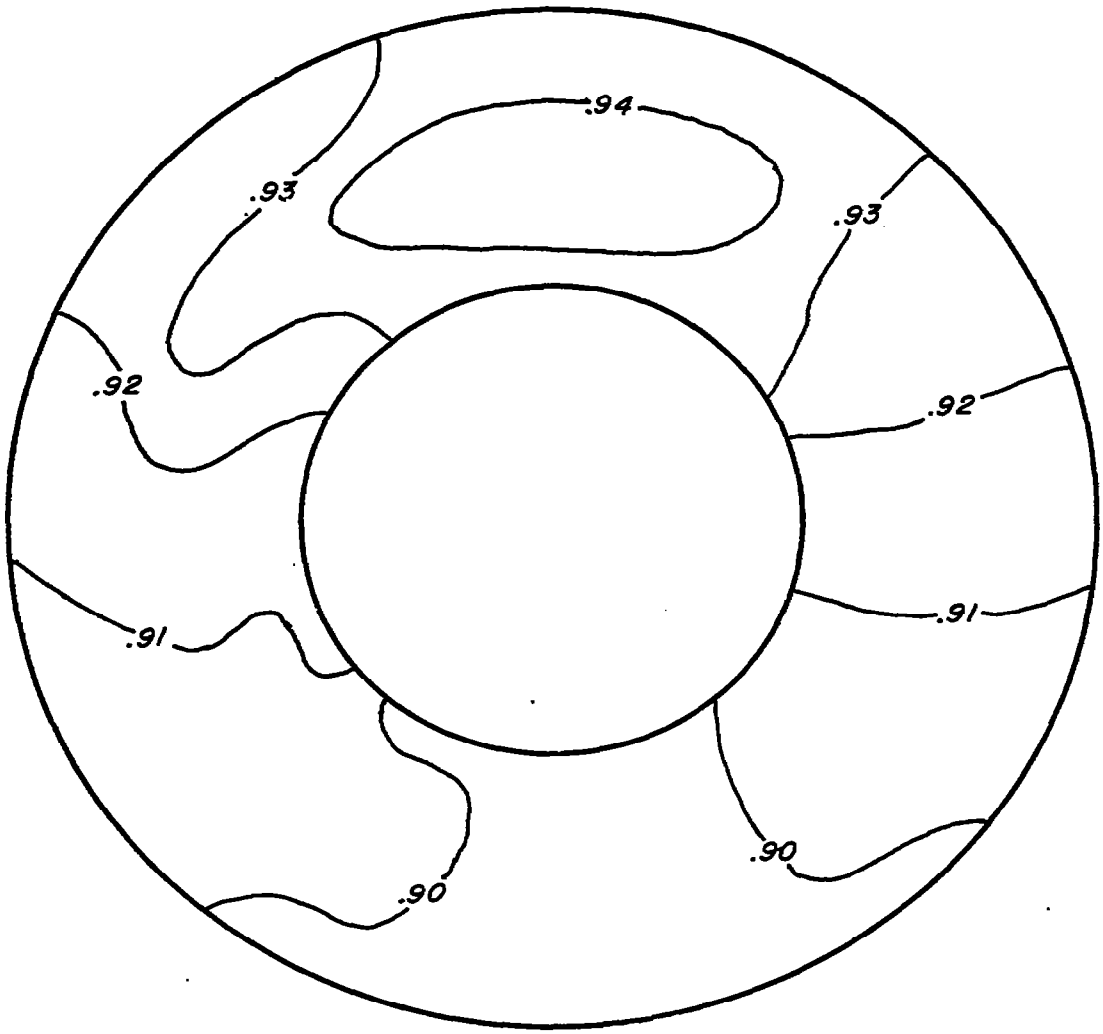

Figure 13.—Distribution of total-pressure ratio, $\frac{H}{H_0}$, at the compressor inlet; $\frac{m_1}{m_0} = \infty$, $M_1 = 0.31$, $\alpha = 0°$, $\beta = 0°$.

[redacted]

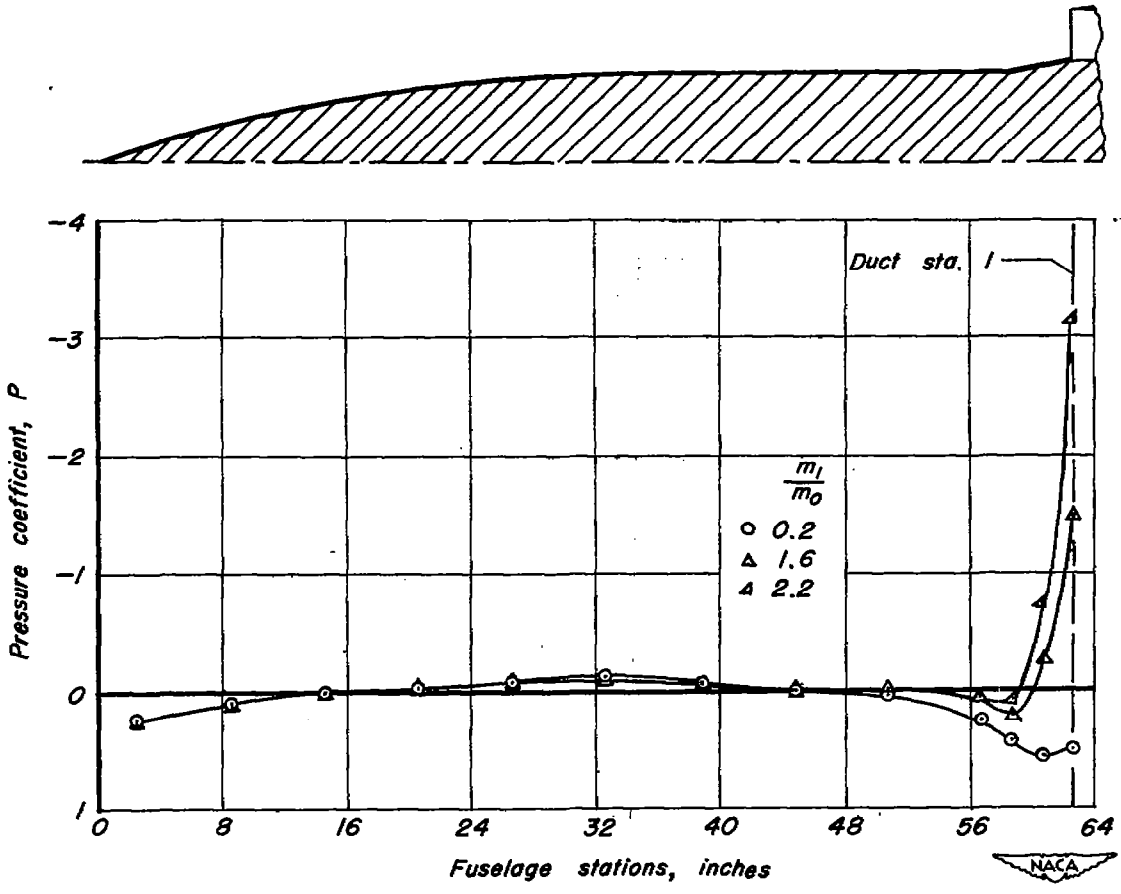

(a) On the forebody.

Figure 14. — The variation of static-pressure coefficient with mass-flow ratio; $\alpha = 0°$, $\beta = 0°$.

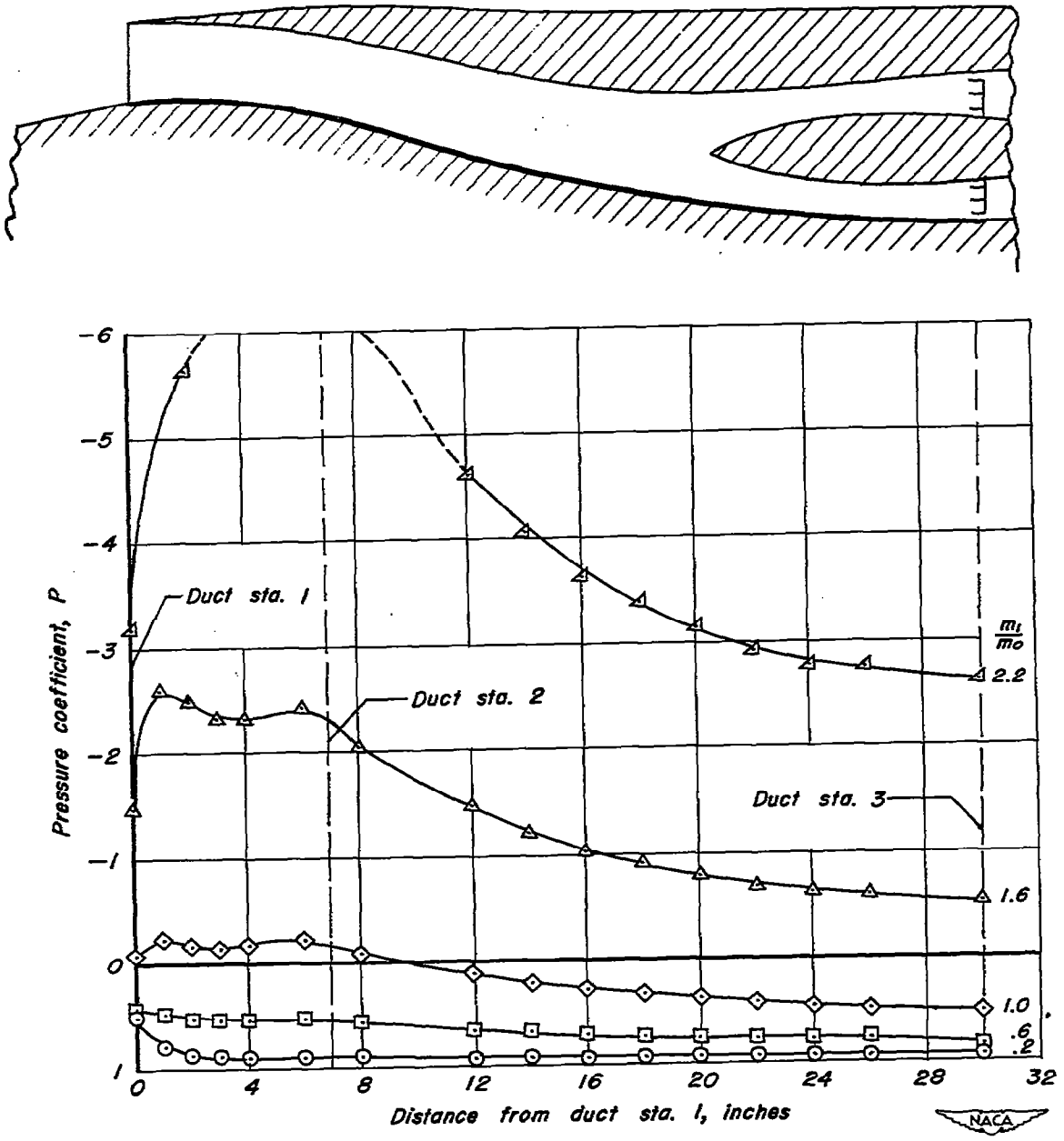

(b) On the duct floor.

Figure 14. —Continued.

[redacted]

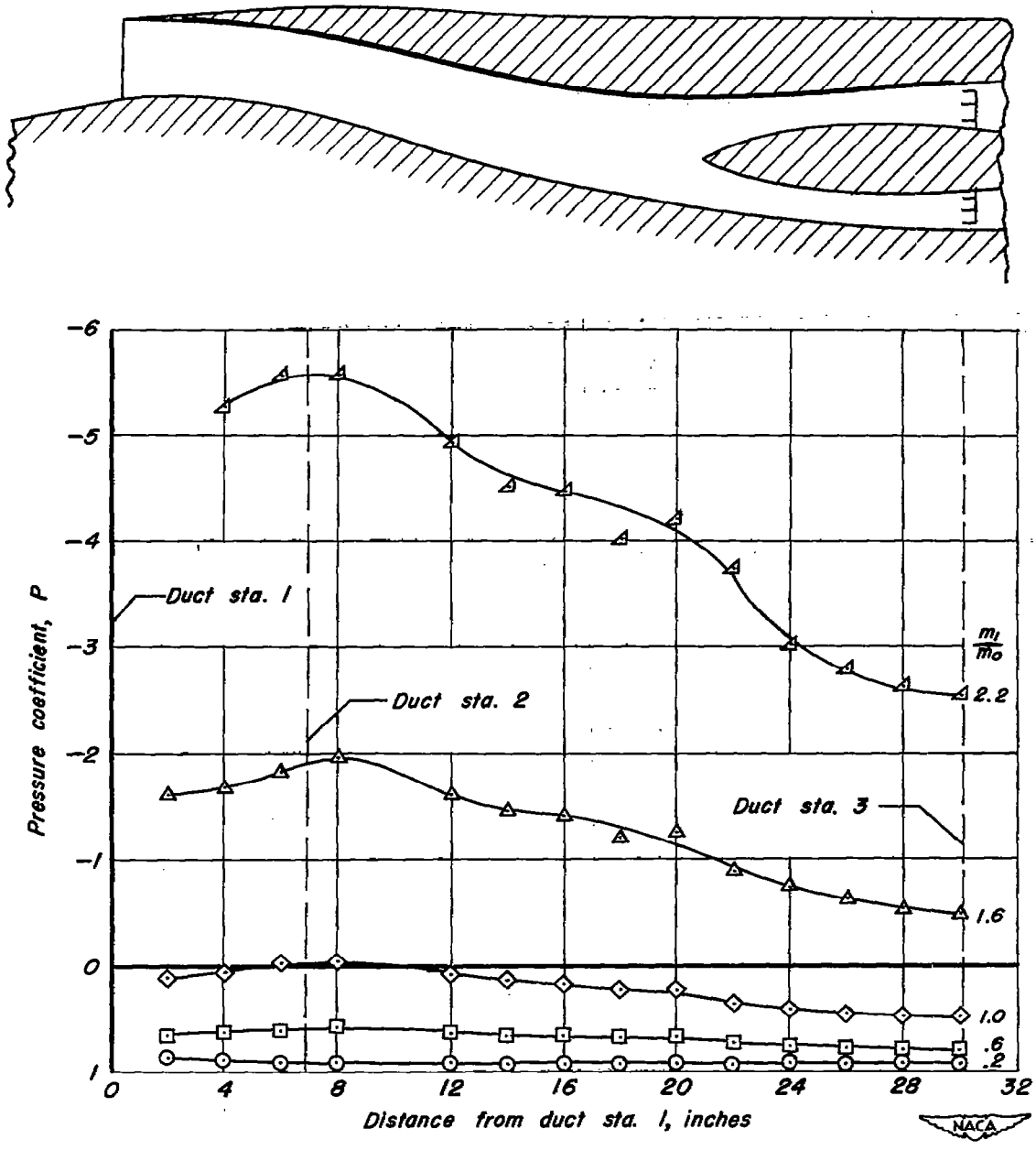

(c) On the duct roof.

Figure 14.—Concluded.

[redacted]

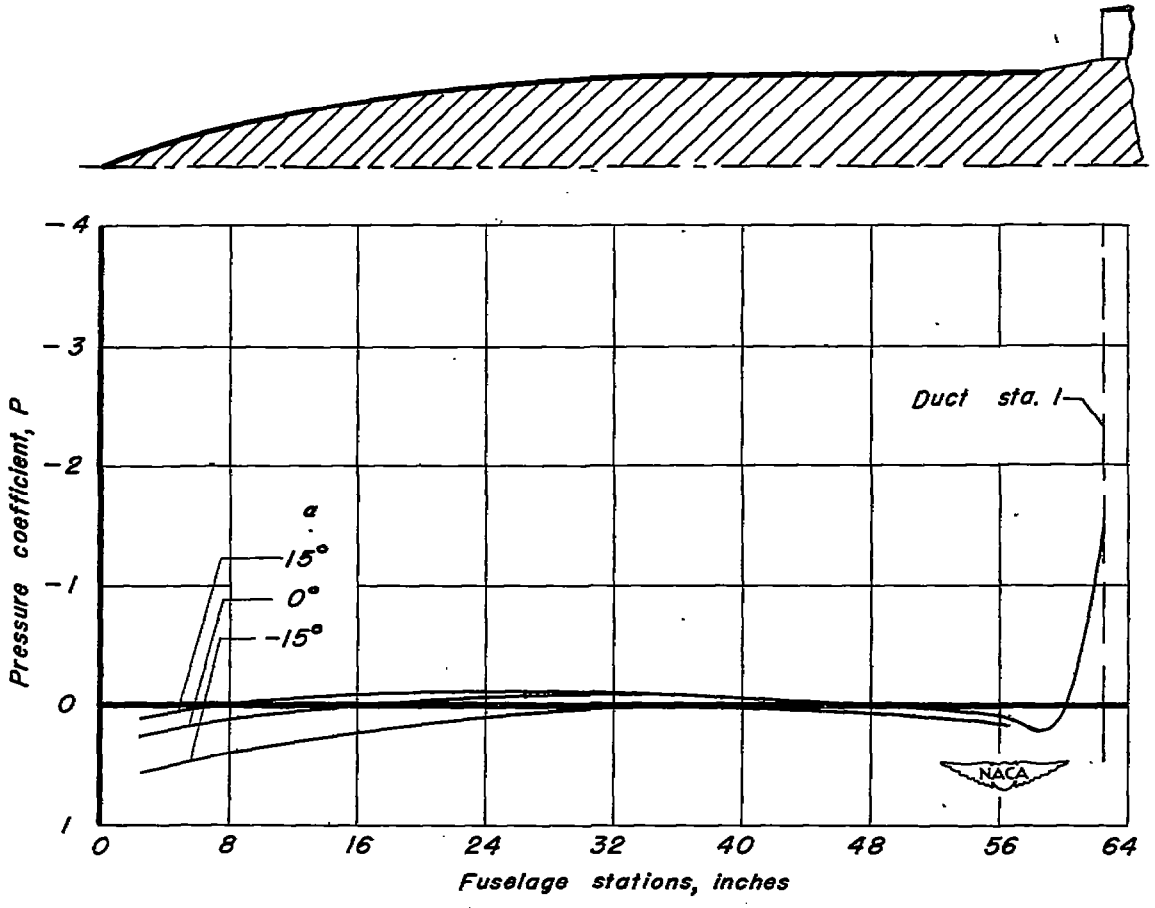

(a) On the forebody.

Figure 15. —The variation of static-pressure coefficient with angle of attack; $\beta = 0°$.

[redacted]

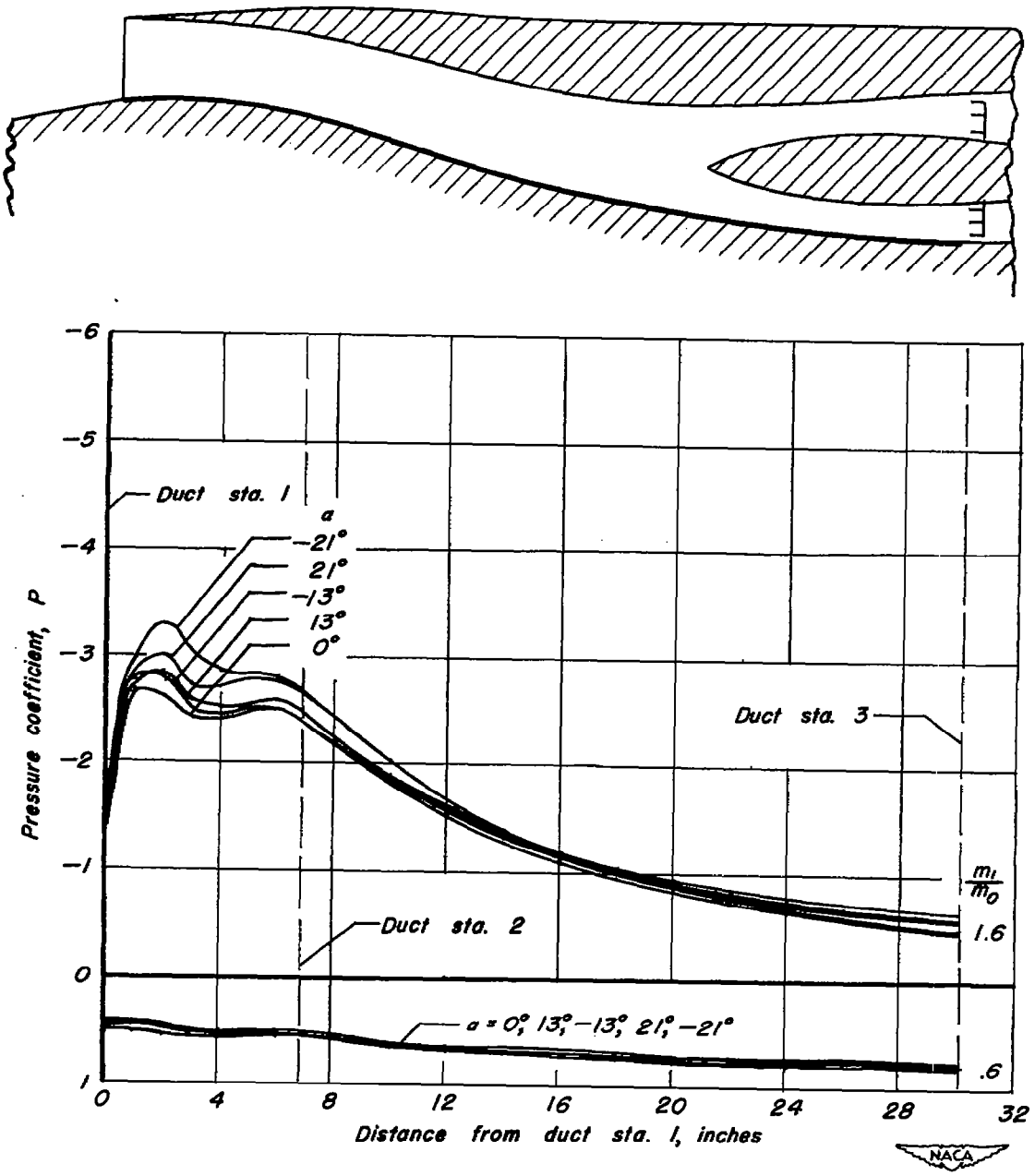

(b) On the duct floor.

Figure 15. —Continued.

[redacted]

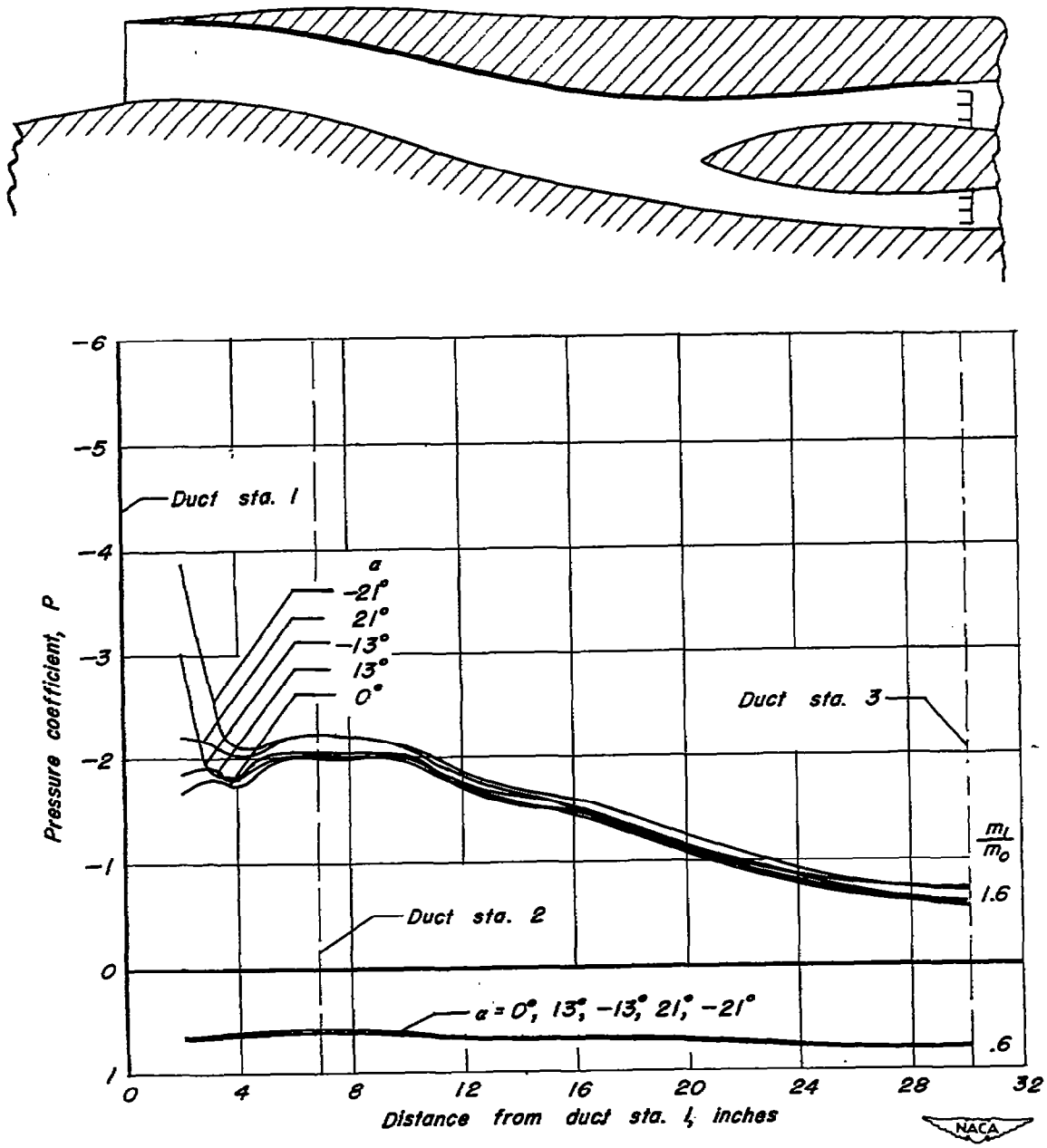

(c) On the duct roof.

Figure 15.—Concluded.

[redacted]

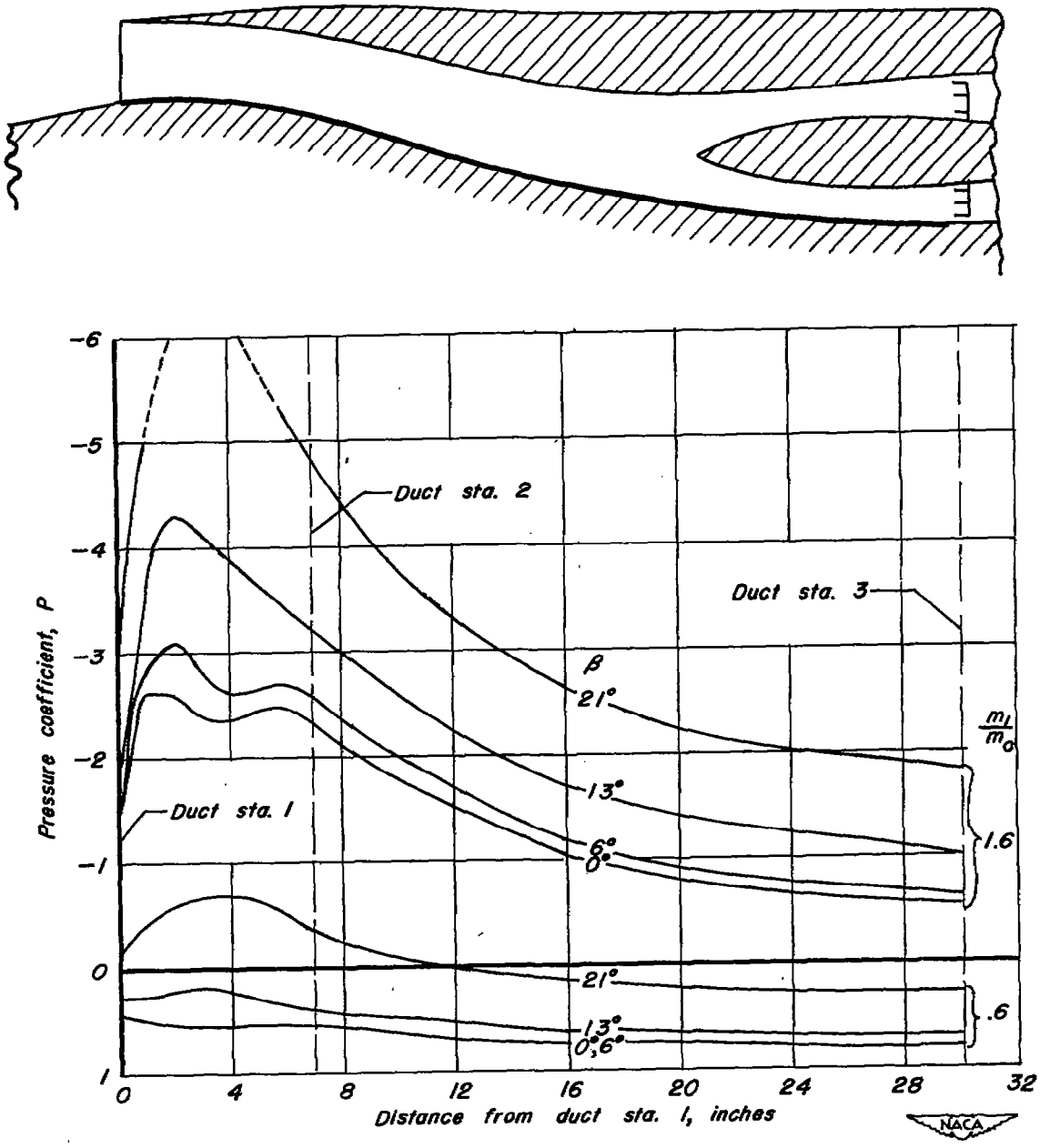

(a) On the duct floor.

Figure 16. — The variation of static-pressure coefficient with angle of sideslip. $\alpha = 0°$.

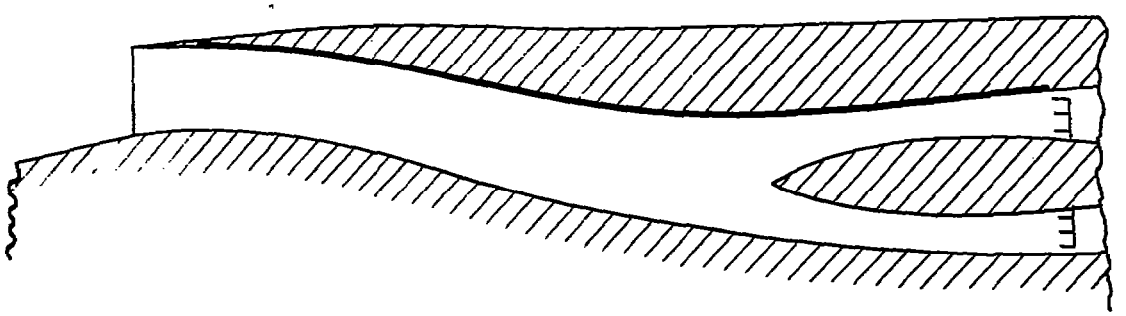

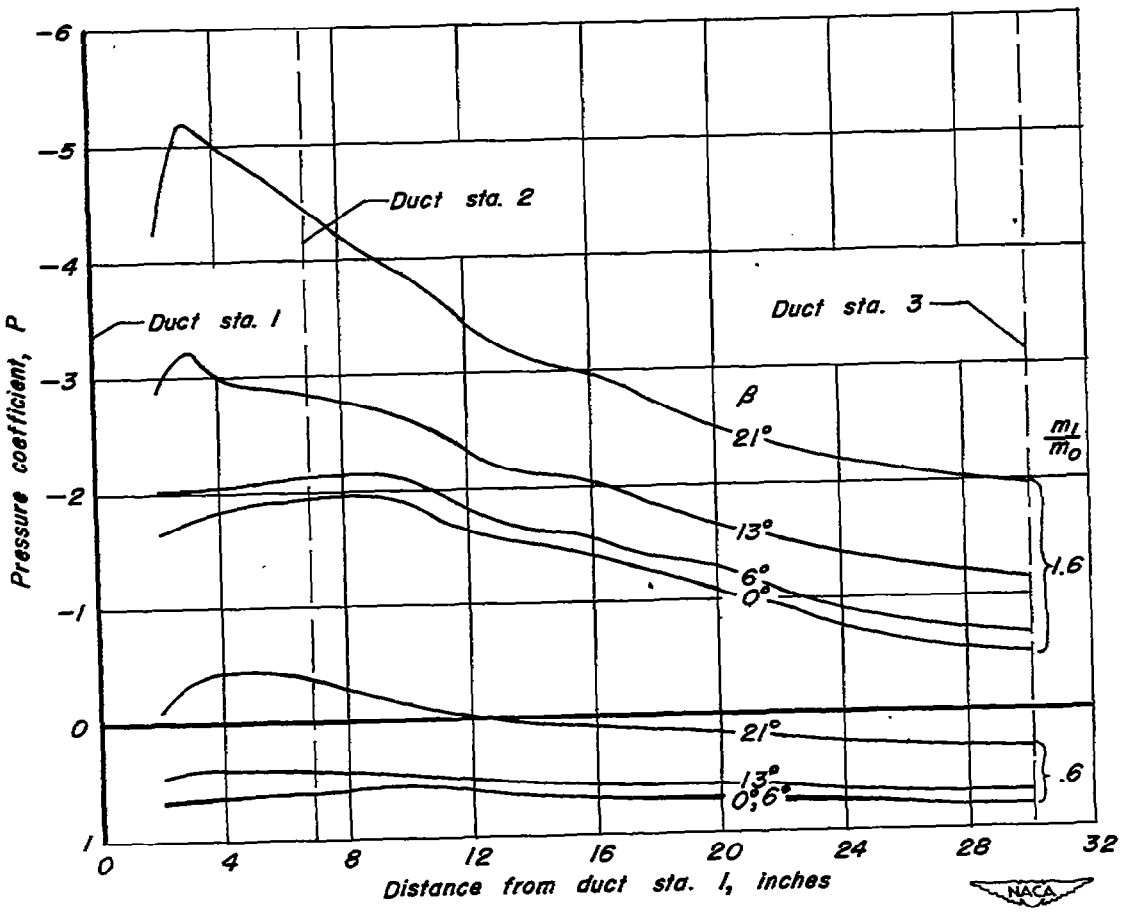

(b) On the duct roof.

Figure 16.—Concluded.

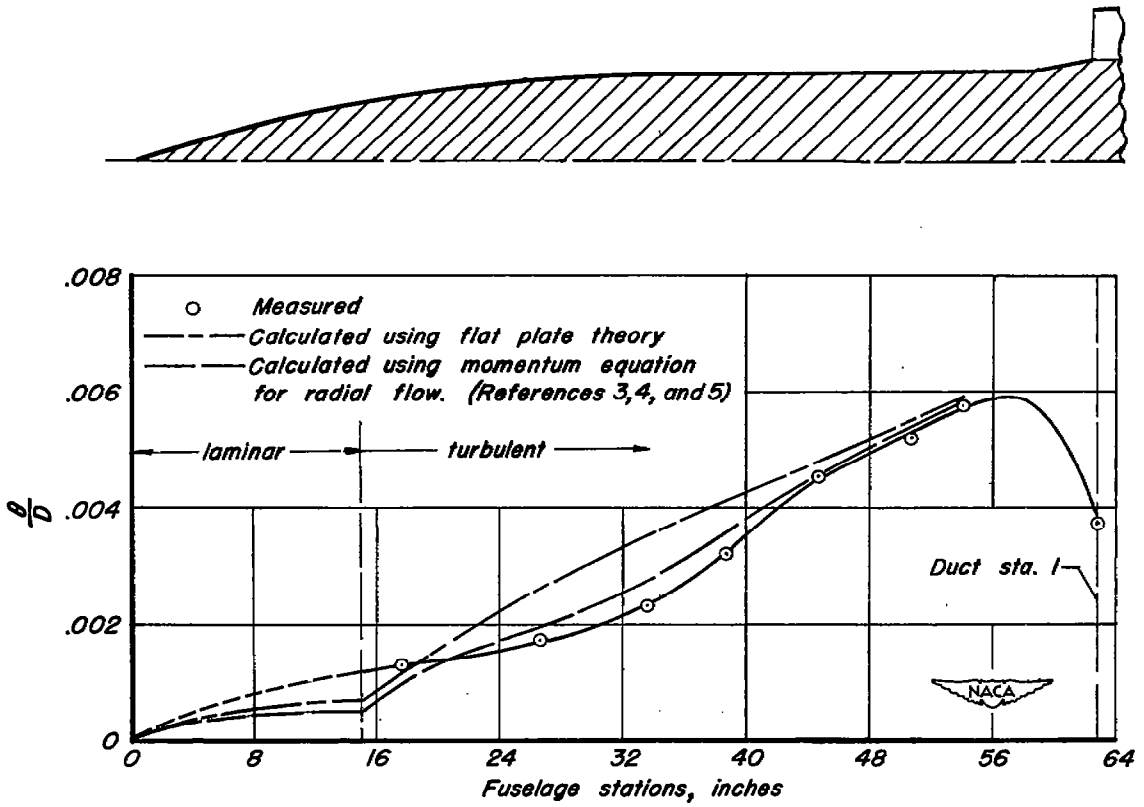

Figure 17.- A comparison of the theoretical with the measured momentum thickness of the boundary layer along the forebody; $\frac{m_1}{m_0} = 1.0$, $\alpha = 0°$, $\beta = 0°$.

[redacted]

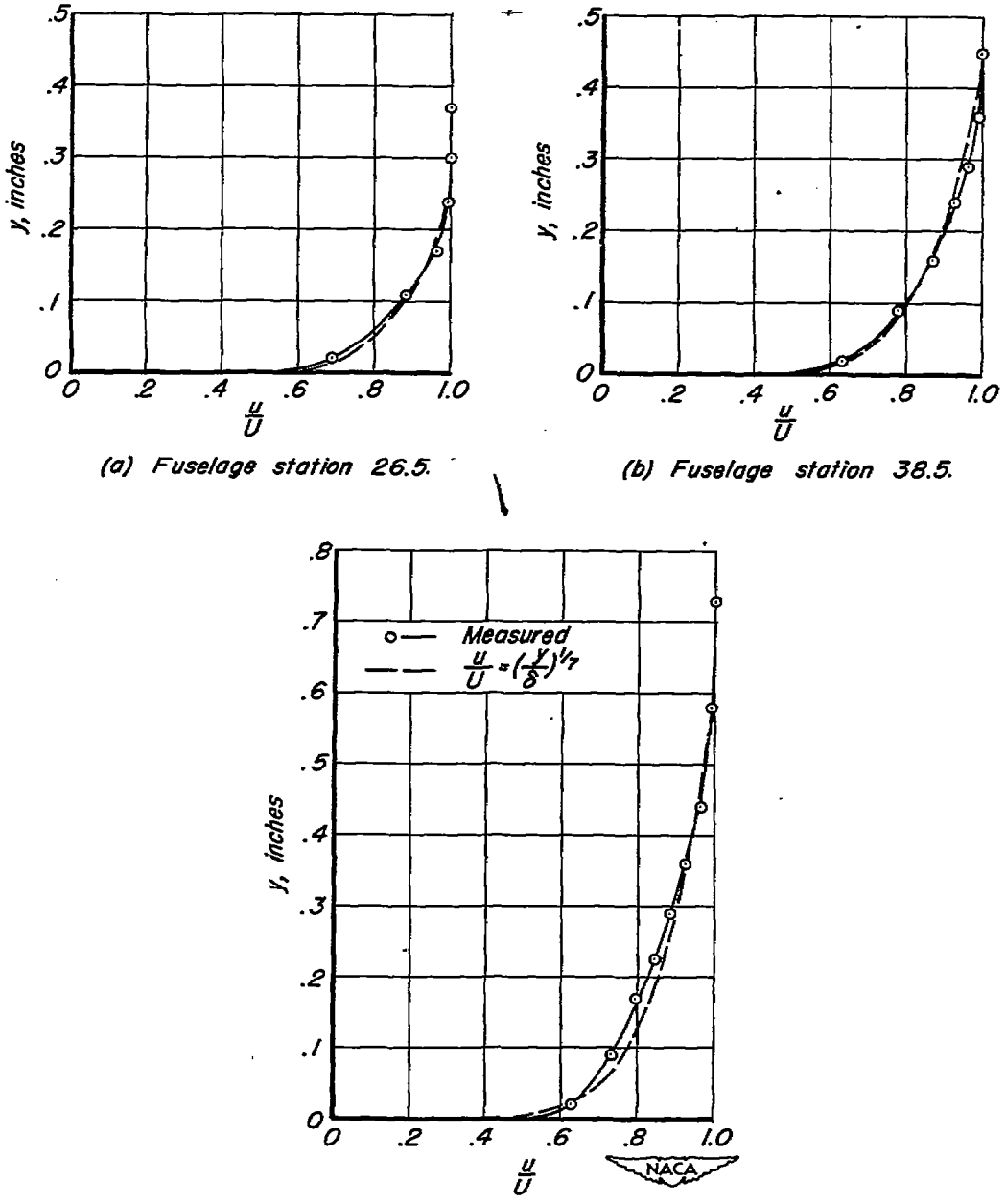

(a) Fuselage station 26.5.

(b) Fuselage station 38.5.

(c) Fuselage station 50.5.

Figure 18.—Boundary-layer profiles at several fuselage stations; $\frac{m_j}{m_0}=1.0$, $\alpha=0°$, $\beta=0°$.

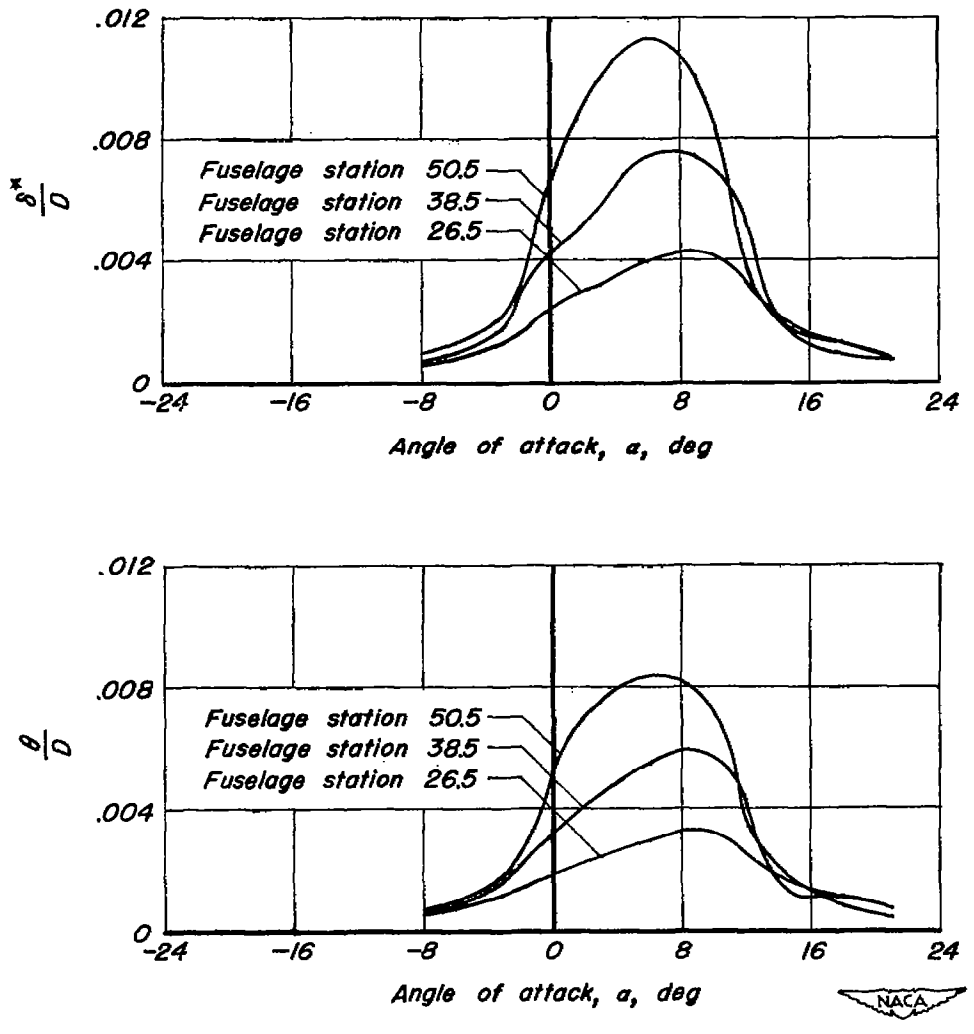

Figure 19. — The variation of displacement thickness and momentum thickness with angle of attack at several fuselage stations; $\frac{m_1}{m_0}=1.0$, $\beta=0°$.

[redacted]

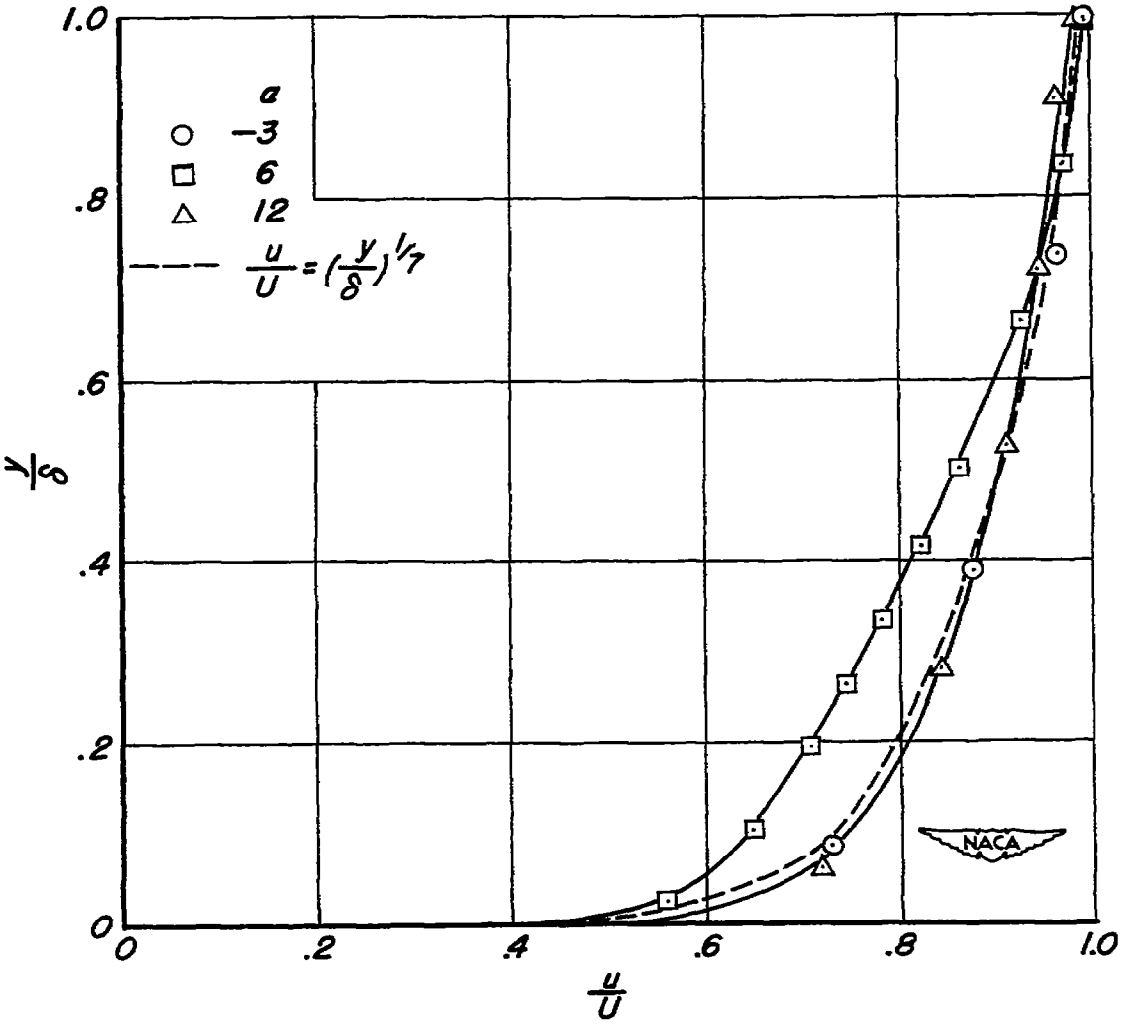

Figure 20.—A comparison of the boundary—layer profiles at fuselage station 50.5 for several angles of attack; $\beta=0°$.

Figure 21.—A sketch of the model at an angle of attack, showing the smoke being entrained in the vortices forming from the forebody. $\beta = 0°$.

45

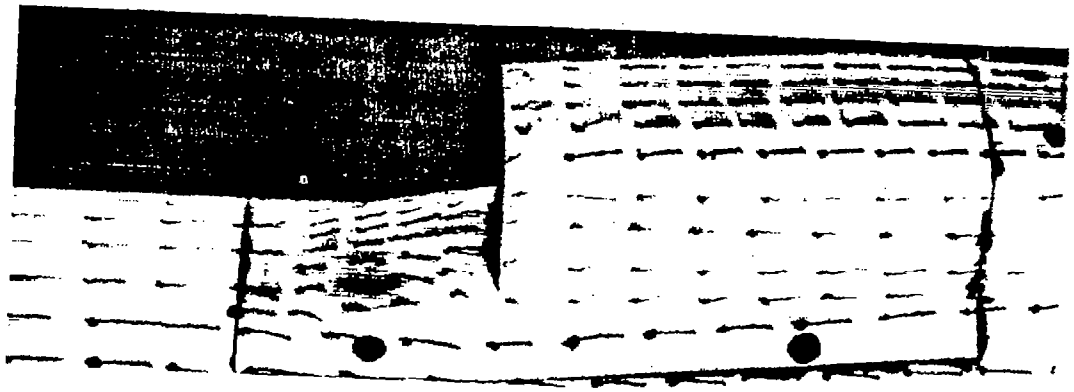

$\frac{m_1}{m_o} = 0.6$

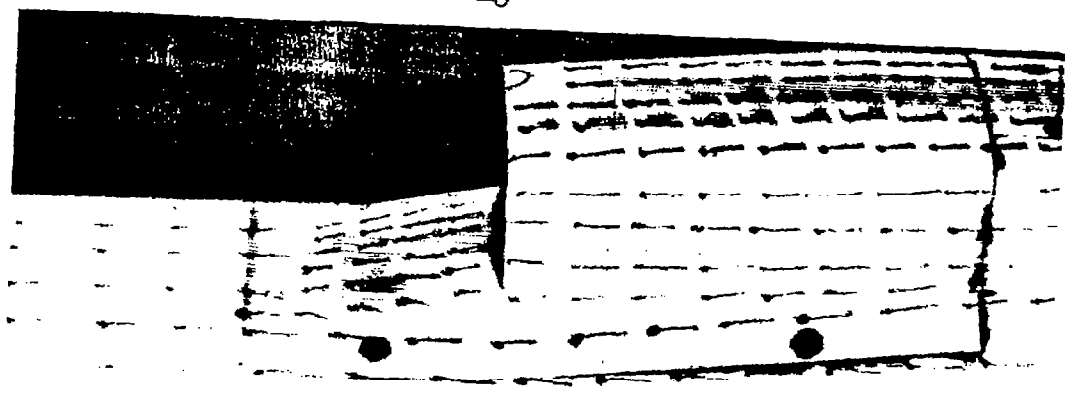

$\frac{m_1}{m_o} = 1.0$

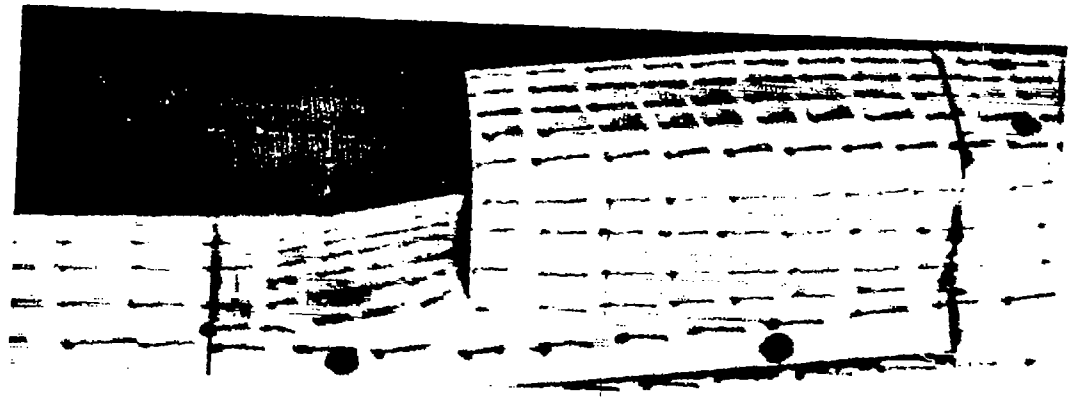

$\frac{m_1}{m_o} = 1.6$

Figure 22.— The effect of mass-flow ratio on the air flow over the exterior of the intake; $\alpha = 0^\circ$, $\beta = 0^\circ$.

NACA-Langley - 7-19-51 - 400